ELSEVIER

Contents lists available at ScienceDirect

# Chemical Engineering Journal

journal homepage: www.elsevier.com/locate/cej





# Coke formation pathway under various reaction conditions during the production of syngas in a dielectric barrier discharge plasma environment using CeO<sub>2</sub> nanorods supported Ni catalysts

Md Monir Hossain a, Md Robayet Ahasan , Xiang Ding b, Ruigang Wang a, \*

#### ARTICLE INFO

Keywords:
Plasma-assisted reforming
Coke formation
CeO<sub>2</sub> nanorods
Tunable diode laser absorption spectroscopy
(TDLAS)
Nano-shaped catalyst

#### ABSTRACT

Plasma-assisted dry reforming of methane (DRM) was investigated using CeO2 nanorods (NR) supported Ni catalysts in a fixed-bed coaxial dielectric barrier discharge (DBD) reactor. This study individually examined the catalyst support, packing material, and 10 wt% Ni-CeO2 NR catalyst under pure thermal and plasma-assisted thermal DRM environments to explore the plasma-thermal synergy. Support and packing material displayed no discernible reactivity under thermal DRM within 450 °C; however, the catalyst exhibited reactivity beginning around 350 °C. Alternatively, plasma-assisted DRM experiments revealed a distinct reaction occurrence at significantly lower temperatures across all sample types. Introducing plasma demonstrated a significant enhancement in CH<sub>4</sub> conversion compared to CO<sub>2</sub> conversion. The 10 wt% Ni-CeO<sub>2</sub> NR catalyst in plasmaassisted DRM testing showed increasing conversions of CH<sub>4</sub> and CO<sub>2</sub> with rising temperatures, peaking at 52.1 % and 46.1 %, respectively, at 450 °C. The catalyst's improved performance in the plasma environment can be attributed to the enhanced metal-support interaction between NiO and the CeO<sub>2</sub> NR support, a consequence of the rich surface oxygen vacancy concentration. However, this increase in conversion was accompanied by an escalation in carbon deposition. Considering contributions from the thermal DRM process, the optimal operating temperature was determined as 350 °C. Increasing plasma power at this temperature led to enhanced conversion. However, beyond a threshold of 23.8 W power, the reaction path altered, resulting in reduced syngas output. Increasing the CH<sub>4</sub>:CO<sub>2</sub> feed gas flow ratio, while maintaining constant plasma power and temperature, elevated H<sub>2</sub>/CO generation. Moreover, increasing the total flow rate under identical conditions, with a constant feed gas flow ratio, reduced both conversions due to decreased chemical residence time. Consequently, under a constant feed gas ratio, a higher syngas yield is achievable with lower overall flow rates.

# 1. Introduction

Nearly 82 % of the world's energy requirements are currently met mainly through the use of fossil fuels, and this proportion is rising rapidly [1]. Meanwhile, significant amounts of greenhouse gases are emitted from these fossil fuels, and the notable contribution comes from  $\rm CO_2$  (76 %), and  $\rm CH_4$  (16 %) [2]. Therefore, it is believed that one of the most challenging obstacles in the twenty-first century is the conversion of greenhouse gases into valuable chemical products [3].

These two leading greenhouse gases can be used in reforming processes, including partial methane oxidation (POM,  $CH_4 + 0.5O_2 = CO + 2H_2$ ) [4-6], dry methane reforming (DRM,  $CH_4 + CO_2 = 2CO + 2H_2$ )

[7–9], and steam methane reforming (SMR,  $CH_4 + H_2O = CO + 3H_2$ ) [10–12]. Recently, the DRM technology has gained the most attention since it uses both greenhouse gases to produce syngas (a mixture of CO and  $H_2$ ) that can be used for gas-to-liquid conversion in the Fischer-Tropsch synthesis process [13] along with some power generation applications. The DRM reaction (Eq. (1)) is highly endothermic, so a highly active catalyst and very high temperatures (600–1000 °C) are required to obtain an effective conversion [14]. The high energy requirement and catalyst deactivation/aging at elevated temperatures make the process commercially incompatible.

$$CH_{4\,(g)} + CO_{2\,(g)} = 2CO_{\,(g)} + 2H_{2\,(g)} \ \, \left(\Delta H_{298K} = +247\,\text{kJ}\,\text{mol}^{-1}\right) \eqno(1)$$

E-mail address: rwang@eng.ua.edu (R. Wang).

<sup>&</sup>lt;sup>a</sup> Department of Metallurgical and Materials Engineering, The University of Alabama, Tuscaloosa, AL 35487, United States

<sup>&</sup>lt;sup>b</sup> College of Urban and Environmental Sciences, Peking University, Beijing 100871, China

<sup>\*</sup> Corresponding author.

Recently, the non-thermal plasma (NTP) catalytic DRM technique has been considered very promising because of its atmospheric pressure and favorable lower operating temperature (<500 °C) alongside reactor compactness and adaptability [15,16]. The primary constituents of NTP are neutral ionized gases, excited species and photons, which catalyze the ionization, dissociation, and excitation of reactants [17]. The neutral ionized gases consist of nonionized gases (such as Ar, N<sub>2</sub>, O<sub>2</sub>), ions (Ar<sup>+</sup>,  $N_2^+$ ,  $O_2^+$ ), and electrons (e<sup>-</sup>), where the positive ions and negative electrons are in equal proportions, hence rendering plasma electrically neutral. However, these ions and free radicals are chemically active to promote subsequent ionization (e-  $+Ar \rightarrow Ar^+ + 2e^-$ ), dissociation (e<sup>-</sup>  $+N_2 \rightarrow 2 N + e^-$ ), excitation (e<sup>-</sup> +Ar  $\rightarrow$  Ar\* + 2e<sup>-</sup>), recombination (e<sup>-</sup>  $+ Ar^+ \rightarrow Ar$ ) and so on. According to the literature [15,18], various types of NTPs have been utilized for DRM. Among them, dielectric barrier discharge (DBD) plasma provides a silent discharge, plasma-separated electrodes, easy incorporation into typical catalysts, and a relatively high conversion rate at low power and temperature, so DBD plasmacatalytic DRM has been a popular choice in various plasma-assisted reactor designs. Combining heterogeneous catalysis with nonequilibrium DBD plasma, plasma-assisted DRM creates a powerful synergy where the catalyst changes the plasma discharge characteristics and lowers the activation barrier for some gas conversion processes [19]. For instance, the highly active catalyst in DRM, nickel (Ni), was incorporated on several supports such as Al<sub>2</sub>O<sub>3</sub>, CeO<sub>2</sub>-Al<sub>2</sub>O<sub>3</sub>, ZrO<sub>2</sub>, ZSM-5, MgO, La $_2$ O $_3$ , SiO $_2$ , SiO $_2$ -Al $_2$ O $_3$ , and tested in DBD environments where the performance varied with strong metal-support interaction (SMSI), dielectric constant value, and active participation of the support [20,21]. Tu et al. [22] examined reduced Ni/Al<sub>2</sub>O<sub>3</sub>, and they discovered that a significant increase in the local electric field and charge deposition on the catalyst surface caused a drop in breakdown voltage from 3.3 kV to 0.75 kV. This change in discharge characteristics also boosts CH<sub>4</sub> and CO<sub>2</sub> conversion up to 18 % and 13 %, respectively, at room temperature and 100 W power, which is possibly due to the uniform dispersion of the conductive Ni active sites. Zhang et al. [23] studied the size of packing materials and catalytic effect under varying plasma power and flow at a constant temperature of 110 °C using various catalysts (Ni/SiO2, NiFe/SiO2 and a mixture of Ni/SiO2 and BaTiO3) as well as catalyst beds (1 and 3 mm dia. BaTiO3 and 3 mm dia. glass). The smaller catalyst bed or packing material (1 mm in dia.) reduces CH4 and CO<sub>2</sub> conversion under constant plasma power (86 W) due to microdischarge energy dissipation. In contrast, the same-sized distinct packing materials have little effect in a plasma DBD environment.

In a plasma-catalytic DRM, more CH<sub>4</sub> and CO<sub>2</sub> conversion typically takes place at high plasma power and low flow rate. This claim was also confirmed using Ni/La<sub>2</sub>O<sub>3</sub> and LaNiO<sub>3</sub> nanoparticles, where Zheng et al. [24] obtained more than 60 % CH<sub>4</sub> and more than 50 % CO<sub>2</sub> conversion at a 50 mL/min (equivalent weight-basis Gas Hourly Space Velocity, WGHSV = 15000 mL/g·h) flow rate, 200 °C temperature, and 200 W plasma power. Adding promoters to catalysts improves catalytic performance in the DBD plasma environment by increasing the number of active sites, stabilizing the catalyst under reaction conditions, and altering the reaction mechanism in some cases. For instance, introducing promoters (K, Mg, and Ce) to the Ni/Al<sub>2</sub>O<sub>3</sub> catalyst improved CH<sub>4</sub> conversion, H2 yield, and energy efficiency of the plasma-assisted DRM [25]. The maximum CO<sub>2</sub> (22.8 %) and CH<sub>4</sub> (31.6 %) conversions were achieved with the Ni-K/Al<sub>2</sub>O<sub>3</sub> catalyst, which technically performed better. However, the Mg-promoted catalyst significantly raised the H<sub>2</sub>/ CO molar ratio (up to 2.2) by reducing CO2 conversion. Additionally, Zeng et al. [25] noticed that more than 80 % of the enhanced carbonaceous species were reactive carbon species, which can be quickly oxidized by carbon dioxide and oxygen atoms and ensure the stability of the catalysts during the reforming event. The strong interaction among catalyst, support, and promoter determines the reaction performance. The degree of reduction and the size of the Ni particles are controlled by the strength of the Ni-support/promoter interaction. In a pure thermal

DRM study, Jang et al. [26] investigated the connection between the kind of support and the Ni particle size, as well as how Ni particle size affects catalytic performance at a particular target temperature. The results showed Ni-MgO-Ce<sub>0.6</sub>Zr<sub>0.4</sub>O<sub>2</sub> had the most considerable oxygen storage capacity (OSC) (2.18  $\times$  10<sup>-4</sup> gmol gcat<sup>-1</sup>) of the catalysts created and the finest performance because of the high reduction degree (83 %) and tiny Ni particle sizes (8.3 nm).

The involvement of CeO<sub>2</sub> as a support or promoter in thermal DRM applications has different advantages, like limiting carbon formation and enhancing catalyst stability due to its oxygen storage capacity and strong interactions with metal oxides and redox characteristics. For example, Laosiripojana et al. [27] limited the carbon formation by adding CeO2 (8 wt%) to Ni/Al2O3, which led to increased activity and stability in thermal DRM. In the investigation, they demonstrated that the prevention of carbon formation happens during the DRM process between adsorbed CH<sub>4</sub>, CO, and the CeO<sub>2</sub> lattice oxygen (O<sub>x</sub>) by CH<sub>4</sub>  $(CH_4 + O_x \rightarrow CO + 2H_2 + O_{x-1})$  and  $CO (CO + O_x \Leftrightarrow CO_2 + O_{x-1})$  surface reactions. It has been reported that high surface area and shape/size controlled CeO2 support can increase the activity and stability of the uniformly distributed metal catalyst clusters. For instance, the shaped CeO<sub>2</sub> nanoparticle was investigated for thermal DRM application by Cardenas-Arenas et al. [28], where they used an 8.7 wt% NiO-CeO<sub>2</sub> nanoparticle catalyst and compared their result with a similar irregularly shaped CeO2 catalyst. The conversion and selectivity of both catalysts were almost identical. However, the shaped CeO2 catalyst was more stable and reduced carbon deposition by 63 % on the catalyst surface compared with the conventional CeO2 catalyst. Li et al. [29] did a comparative investigation of how differently shaped CeO2 nanoparticles interact with the Ru catalyst, and finally, they correlated the exposed surface planes of CeO2 nanoparticles with CO oxidation activity. The presence of oxygen vacancies within the support additionally introduces mechanistic bifunctionality, enabling CO2 activation at support sites. This phenomenon facilitates the adsorption and dissociation of CH<sub>4</sub> on metal sites while helping to maintain the metal nanoparticles in their reduced state, which is known to be a more active phase for noble metals in DRM reactions [30]. To our best knowledge, various nano-shaped CeO2 supported catalysts in a plasma-assisted DRM environment have not been investigated before. Our hypothesis is that different-shaped CeO2 should interact with plasma differently due to exposed crystal planes, oxygen storage capacity, and distinct Ce<sup>3+</sup>/Ce<sup>4+</sup> redox chemistry.

In this study, we focused on a highly active Ni catalyst on  ${\rm CeO_2~NR}$  support, where the exposed facet (110)/(100)/(111) have either lower oxygen vacancy formation energy or a higher number of surface defects, resulting in an enhanced metal support interaction (MSI) [29,31–35]. In this aspect, the catalyst-support properties, support morphology, and plasma-catalyst interactions were investigated. The plasma DRM performance was compared for plasma alone, plasma with support, and plasma with catalyst. The plasma DRM performance was further analyzed under different temperatures, feed gas flow, and applied plasma power to better understand the overall reaction mechanisms under various circumstances.

## 2. Experimental section

# 2.1. Catalyst preparation

The  $CeO_2$  NR support was prepared via a simple hydrothermal method, as described in previous work [29,36] from our research group. In hydrothermal synthesis, 8 mL of 6.0 M NaOH solution was added dropwise into 88 mL of  $Ce(NO_3)_3 \cdot 6H_2O$  (0.1 M) solution in a 200 mL Teflon liner under vigorous stirring, and then the mixed solution was further stirred for around 20 s. The mixed solution in the Teflon liner was sealed in a stainless-steel autoclave and kept for 48 h at 90 °C, and the nanorod-shaped  $CeO_2$  sample was formed. The obtained sample was filtered, washed with enough deionized (DI) water (typically 700 mL)

and 20 mL ethanol, and then dried at 80  $^{\circ}$ C for 20 h to remove water. To further prepare the sample, the dried material was meticulously ground using a mortar and pestle, thereby synthesizing the desired CeO<sub>2</sub> NR powder support.

A coprecipitation method shown in Fig. 1 was employed to prepare the NiOx/CeO2 NR catalyst, where the prepared CeO2 NR support powder was mixed with DI water and stirred in a beaker at around 60 °C. The precipitating agent NH<sub>4</sub>(OH) (1.0 M) aqueous solution and the aqueous precursor Ni(NO3)2·6H2O solution were then added concurrently dropwise into the CeO2 NR and DI water mixer while maintaining the solution's pH of 9.0  $\sim$  9.5. The precipitated solution was further homogenized at around 60 °C for 24 h, followed by filtering and washing with DI water and ethanol. The washed sample was dried at 80  $^{\circ}\text{C}$  for 20 h to remove any residual water and get the solid Ni doped CeO2 NR. The dried solid solution was meticulously pulverized using a mortar and pestle, resulting in a fine powder. This powder was subsequently subjected to calcination in a box furnace at 450 °C for 6.5 h, ultimately yielding the desired final catalyst consisting of Ni-based nanoparticles supported on CeO<sub>2</sub> NR. The prepared sample had a 10 wt% Ni loading, so the sample was designated as 10 wt% Ni-CeO<sub>2</sub> NR. The coprecipitation method was also used to synthesize pure NiO catalyst, as discussed in the supplementary section.

#### 2.2. Catalyst characterization

The crystallinity and crystal structure of the prepared samples were determined by powder X-ray diffraction (XRD) technique, and the samples were tested on a Philips X'Pert MPD diffractometer (Cu K $\alpha$  radiation ( $\lambda=1.5418$  Å)) and the 20 range was in between 10° and 90°. The samples' Raman spectra in the range of 200 to 1400 cm<sup>-1</sup> were obtained using a Horiba Labram HR 800 Raman Spectrometer (laser wavelength 532 nm) to examine the cell deformities and oxygen vacancies. Single point Brunauer-Emmett-Teller (BET) surface area and hydrogen temperature programmed reduction (H<sub>2</sub>-TPR) were examined on a Micromeritics AutoChem II 2920 chemisorption analyzer. The nitrogen (N<sub>2</sub>) adsorption/desorption method was used to measure the BET surface area, where the signal was collected using a thermal conductivity detector (TCD) at around 80 K. The reducibility properties of catalyst and support were investigated in the H<sub>2</sub>-TPR experiments,

where a mixture of  $\rm H_2$  and Ar (10 and 90 % by volume, respectively) flowed into a quartz tube containing sample. The peak area method, calibrated using a reference  $\rm Ag_2O$  sample, was used to calculate how much  $\rm H_2$  was consumed in the reduction process [37]. A JEOL 7000F scanning electron microscope (SEM) with an energy-dispersive X-ray spectroscopy (EDS) detector was used to obtain the synthesized samples' particle morphology/agglomeration, particle sizes, and chemical compositions. The morphology of individual nano-shaped catalysts was observed in a Tecnai F20 transmission electron microscope (TEM).

#### 2.3. Experimental setup and catalytic reaction

The DRM performance was observed by testing the catalysts in a coaxial tube fixed-bed flow DBD reactor system. The schematic diagram of the plasma DRM catalyst testing system is shown in Fig. 2, together with a flow diagram and a gas detection system. The testing system can be divided into three sections: flue gas analysis, DBD reactor, and gas supply. Gases from Airgas (purity > 99.99 %) are fed to the reactor by mass flow controllers (Brooks GF040 Multiflo MFC, response time 1 sec) in the gas supply section. The coaxial DBD reactor consists of two concentric quartz tubes that are positioned inside an ATS 3210 furnace with a maximum temperature capability of 1200 °C. The outer quartz tube has a constant diameter of 25.4 mm, while the open-ended inner quartz tube (OD = 6.35 mm) features an expansion portion (ID = 9.40mm, Length = 89.9 mm). To generate plasma in the reactor, one electrode (Kanthal A-1 wire, 24 g) is positioned at the center axis of the tubes. The wire (Kanthal A-1 wire, 32 g) is wrapped around the inner tube's expansion section for another electrode. The center electrode is covered with a nonporous alumina ceramic tube, which forms a dielectric barrier. The electrodes' discharge gap measured  $6.12\,\mbox{mm}$  . The catalyst material is placed inside the inner expansion section of this reactor part dispersed with quartz wool, and the plasma is created in this expansion section.

The flue gas analysis system analyzes flue gases, where some gases (CO,  $H_2$ ,  $CH_4$ ,  $CO_2$ , Ar) are detected by a quadrupole mass spectrometer (QMS, Extrel MAX300-EGA, 300 ms, 1–250 amu detectability), and some other gases (higher hydrocarbons like  $C_2H_6$ ) are detected using a custom-designed IR tunable diode laser absorption spectroscopy (TDLAS) system. The TDLAS system component includes a quantum

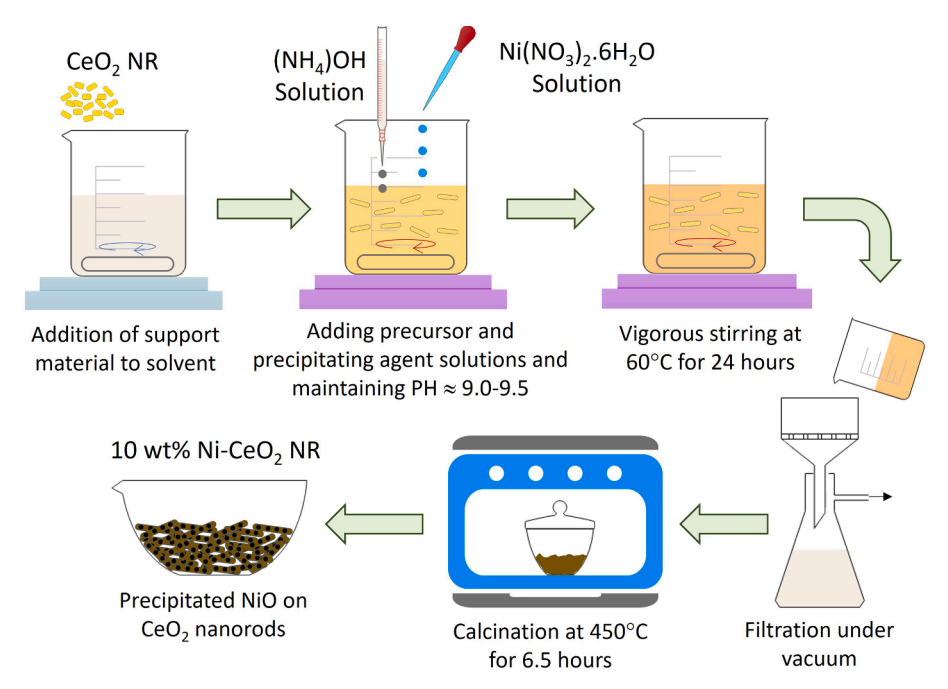


Fig. 1. Synthesizing steps of 10 wt% Ni-CeO<sub>2</sub> NR catalyst via coprecipitation method.

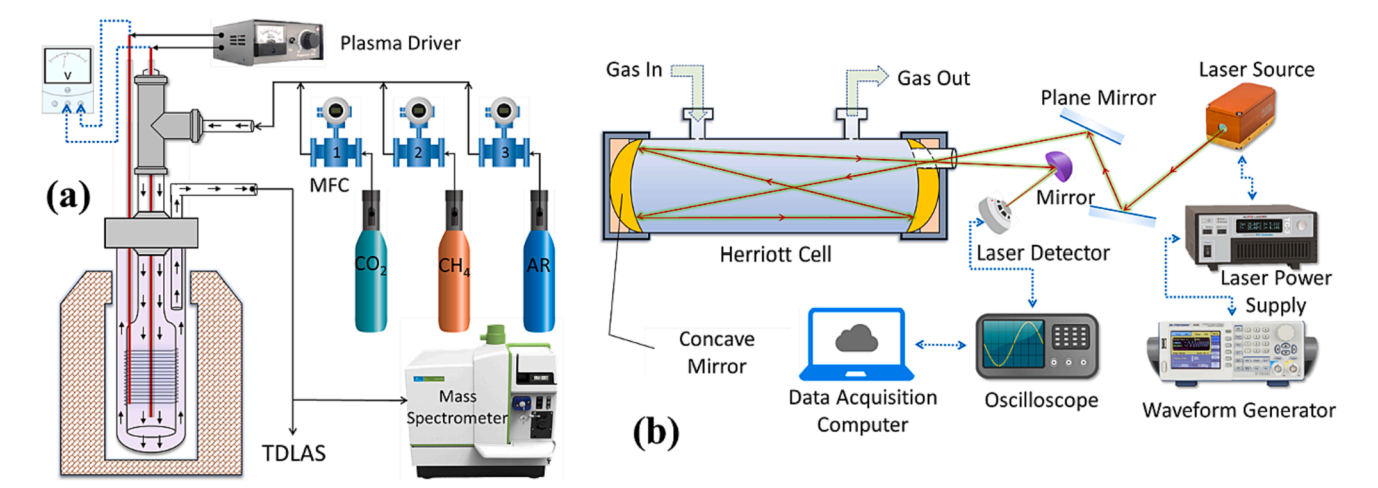


Fig. 2. (a) Experimental setup of DBD plasma reactor system and (b) Quantum cascade laser absorption spectroscopy system.

cascade laser (QCL) (Alpes Laser, sbcw6200 DN) with a controller as laser supply, a handmade Herriott cell to increase gas absorption length, an IR detector to detect laser signal or intensity, an oscilloscope (Tektronix TBS1154, 150 MHz), and a waveform generator (B&K Precision, 4055B, 1 Hz to 60 MHz). The precision of this system was tested before in the oxidative coupling of methane reaction [38].

In the DBD plasma DRM reactor system, CH<sub>4</sub> and CO<sub>2</sub> have flown as the main feed gases. Before and after the experiment, Ar gas clears or neutralizes the reactor from other contaminated gases. Separate MFCs are used to regulate each type of gas flow, and the gases are mixed in a mixing chamber before entering the reactor. The furnace controls the temperature in the reaction zone, which ranges from 100 to 450 °C with a 4 °C/min ramp. An AC high-voltage power supply (PVM500-2500 from Amazing1.com) with a peak-to-peak voltage of 40 kV and frequency of 20-70 kHz is connected to the DBD reactor to generate uniform plasma. The power supply frequency for this study was set at 23.3 kHz. The electrical signals (applied voltage and current) were recorded on the same oscilloscope that was connected to the TDLAS system using a high-voltage probe (Tektronix P6015A) and a current transformer (Magnelab, CT-E 0.5 BNC). The plasma driver's duty cycle was used to manually regulate the supplied plasma power. The gas sample was taken from the reactor and sent to the QMS and QCL absorption spectroscopy systems. The flue gas analysis was continuous, and data was logged into an integrated data collection system.

#### 3. Result and Discussion

#### 3.1. Catalyst Structure, Property, and reducibility

The powder XRD patterns in Fig. 3(a) confirm the crystal structures of the bare  $CeO_2$  NR support and the  $CeO_2$  NR supported Ni catalyst. The diffraction peaks 20 found at  $28.6^{\circ}$ ,  $33.1^{\circ}$ ,  $47.5^{\circ}$ ,  $56.3^{\circ}$ ,  $59.1^{\circ}$ ,  $69.4^{\circ}$ ,  $76.7^{\circ}$ ,  $79.1^{\circ}$ , and  $88.5^{\circ}$  are allocated to face-centered cubic fluorite  $CeO_2$  (PDF# 34–0394), and these peaks are present in both  $CeO_2$  NR support and 10 wt% Ni-CeO<sub>2</sub> NR catalyst. After incorporation of Ni onto the support and calcination at  $450~^{\circ}C$ , the additional 20 peaks are found at  $37.2^{\circ}$ ,  $43.3^{\circ}$ , and  $63.9^{\circ}$  in the 10 wt% Ni-CeO<sub>2</sub> NR catalyst, and these correspond to the characteristic peaks of the NiO phase (PDF# 47–1049). The low intensities of NiO peaks indicate good dispersion of Ni particles throughout the support [39].

The Raman spectra for  $CeO_2$  NR support and 10 wt% Ni-CeO<sub>2</sub> NR catalyst are shown in Fig. 3(b). In  $CeO_2$  NR support, the most substantial peak near 457 cm<sup>-1</sup> attributes to the vibration model of octahedral local symmetry  $(F_{2g})$  from the  $CeO_2$  lattice [33,40]. Additional modes present include the second-order transverse acoustic mode (2TA) at 255 cm<sup>-1</sup>, defect-induced mode (D) at 596 cm<sup>-1</sup>, and second-order longitudinal optical mode (2LO) at 1184 cm<sup>-1</sup> [32,41,42]. The ratio of the D-band (representing oxygen sublattice disorder) to the  $F_{2g}$  mode provides insight into the oxygen vacancy density, as summarized in Table 1. The oxygen vacancy concentration has a significant value for the NR support, which increases upon incorporating Ni into the support. The incorporation of Ni and intense interaction with the  $CeO_2$  NR support weakened

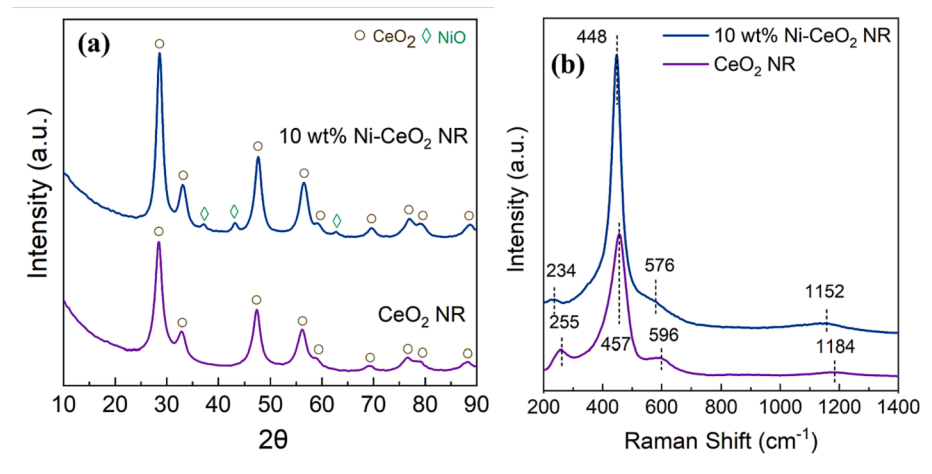


Fig. 3. (a) XRD patterns and (b) Raman spectra of CeO<sub>2</sub> NR support and 10 wt% Ni-CeO<sub>2</sub> NR catalyst.

**Table 1**Measured and calculated properties of support and catalyst.

Sample	Crystallite Size (nm)	BET Surface Area (m²/g catalyst)	Oxygen Vacancy Concentration ( $I_D/I_{F2g}$ )	H <sub>2</sub> consumption (μmole/g)
CeO <sub>2</sub> NR	4.4	114.1	0.21	485.1
$10 \mathrm{\ wt\%}$ Ni- $\mathrm{CeO}_2$ NR	5.6	145.1	0.31	1988.6

the Ce-O symmetry bond, reflected in the  $F_{2g}$  peak shifting from 457 to 448 cm<sup>-1</sup> [43,44]. The 2LO peak in the Ni-CeO<sub>2</sub> NR catalyst broadened and shifted from 1184 to 1152 cm<sup>-1</sup> specifying CeO<sub>2</sub> lattice distortion and formation of Ni-O-Ce solid solution due to Ni incorporation [43,45].

The average crystallite sizes and BET surface areas of support and catalyst are listed in Table 1, where the crystallite sizes are calculated from the XRD results considering the peak broadness of  $CeO_2$  (111) via Scherrer equation. The crystallite size for the  $CeO_2$  NR support is 4.4 nm, which increases to 5.6 nm after Ni incorporation on the support. Adding Ni to the support also increases the BET surface area. According to the XRD patterns, the excellent dispersion of Ni particles, which avoids particle aggregation, may be the reason for increasing the surface area [40].

The interaction between Ni species and CeO2 NR support and reducibility was evaluated through the H2-TPR experiment. Fig. 4 exhibits H2-TPR profiles of CeO2 support, 10 wt% Ni-CeO2 catalyst, and pure NiO catalyst, where hydrogen (H2) reduced the catalysts and prominent peak area determined H2 consumption. Around 90 mg of samples were examined in each instance to evaluate the reducibility. The CeO<sub>2</sub> NR support primarily exhibits two prominent H<sub>2</sub> consumption peaks, one at roughly 475  $^{\circ}$ C and the other at around 766  $^{\circ}$ C. The first peak attributes to the surface CeO<sub>2</sub> reduction into CeO<sub>2-x</sub>, and the second peak corresponds to bulk CeO<sub>2</sub> reduction from Ce<sup>4+</sup> to Ce<sup>3+</sup> [34,46]. Pure NiO has only a single reduction step at 365 °C associated with bulk crystalline NiO phase reduction to metallic Ni [35,47]. After incorporation of Ni to the support, for 10 wt% Ni-CeO2 NR, there are four hydrogen consumption peaks noticed at 172, 208, 300, and 776 °C and these are allocated as  $\alpha_1$ ,  $\alpha_2$ ,  $\beta$ , and  $\delta$  peaks, respectively. The lowintensity δ peak at 776 °C is ascribed to bulk CeO<sub>2</sub> reduction, which is shifted from 766 °C, possibly due to the presence of some Ni, which

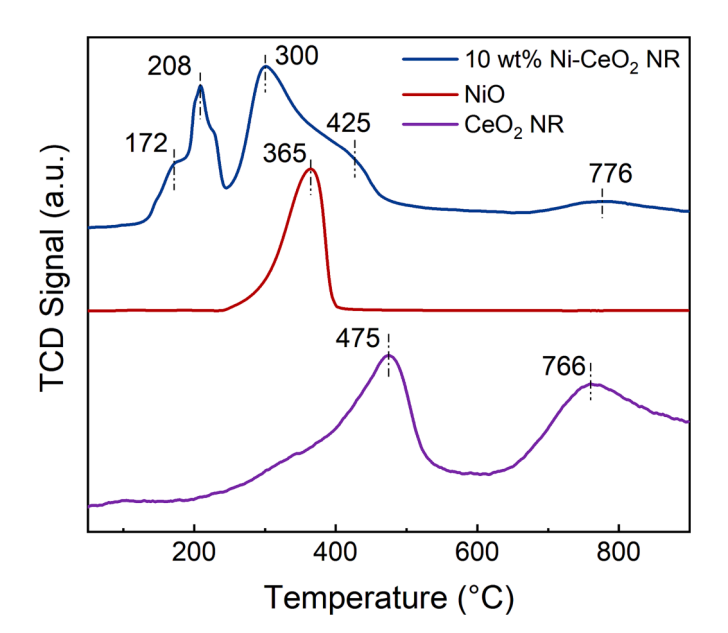


Fig. 4.  $H_2$ -TPR profiles of  $CeO_2$  NR support, pure NiO, and 10 wt% Ni-CeO<sub>2</sub> NR catalyst (unequal y-axis scaling).

forms a bimetallic Ni-Ce bond. The low-temperature  $\alpha_1$  and  $\alpha_2$  peaks at 172 and 208 °C, respectively, can be attributed to the reduction of highly dispersed NiO species that weakly interact with the support [48,49]. The  $H_2$  consumption peak  $\beta$  found at 300 °C due to the reduction of NiO particles; in the case of pure NiO, this peak was at 365 °C. An additional shoulder peak, observed in conjunction with the  $\beta$  peak at approximately 425 °C, can be attributed to the surface reduction of CeO<sub>2</sub>. This reduction event is typically observed at 475 °C for pristine CeO<sub>2</sub> support. Both 300 and 425 °C reduction peaks are assigned to the solid solutions of NiO-CeO<sub>2</sub>, indicating a strong interaction between the two, which could be NiO-doped CeO2 and/or CeO2-doped NiO. However, the presence of nickel catalysts facilitates the reduction of surface CeO2, notably the Ce<sup>4+</sup> ions, resulting in a shift of this peak to lower temperatures [50]. The total amount of H<sub>2</sub> consumption is also mentioned in Table 1, and it was calculated using the peak-area method, where the calibration was performed using various masses of standard Ag<sub>2</sub>O sample, considering the complete reduction reaction  $(Ag_2O + H_2 = 2Ag + H_2O)$  [37]. The oxygen vacancies, particle size, particle dispersions, and interactions between the support and catalyst explained by the XRD, Raman, and TPR data all agree with one another.

Fig. 5 shows images of the 10 wt% Ni-CeO $_2$  NR particles and information about the catalyst's shape, elemental composition, and elemental distribution. The TEM image in Fig. 5(a) demonstrates the nanorod shape of the catalyst with exposed crystal planes. The lengths of the rods range from 35 to 90 nm, with diameters of 5 to 10 nm. The SEM micrograph in Fig. 5(b) illustrates the relative sizes of the catalyst particles and showcases their agglomeration. The EDS spectrum in Fig. 5(g) identifies the elements present in the catalyst, including the substrate carbon tape, while confirming their relative weight percentages. The EDS mapping in Fig. 5(c-f) shows that Ni is distributed uniformly throughout the catalyst, which is critical for DRM application. These microscopic characterizations align with previous findings and provide further evidence of the homogeneous Ni distribution and the strong interaction between Ni and CeO $_2$  NR.

#### 3.2. Catalysis: Dry methane reforming performance

The DRM performance was utilized by testing the catalyst and measuring output gas species in the DBD plasma experimental setup. In the DBD reactor section, the catalyst (mass = 200 mg) to be tested was put inside the reactor and distributed with quartz wool (dielectric constant 3.76), functioning as a holding or packing material. The reactor volume, where the catalyst is positioned and plasma is generated, measures 6.24 cm<sup>3</sup>. Regardless of the test type (pure thermal or plasmaassisted DRM) or sample (CeO2 NR or 10 wt% Ni-CeO2 NR), the quartz wool packing material was always present in the reactor. The samples were the subject of numerous experiments using various reaction settings. The reaction parameters included a temperature range of 100 to 450 °C, a total flow range of 150 to 500 cm<sup>3</sup>/min, a feed gas flow ratio (CH<sub>4</sub>:CO<sub>2</sub>) range of 0.4 to 2.5, and a plasma power range of 8.3 to 27.1 W. In all cases, a plasma voltage of about 11.8 kV was applied (peak-topeak). The voltage and current waveforms recorded from the oscilloscope are directly integrated to determine the average applied plasma power as described in the literature [51], and sample waveforms are shown in Fig. S5. Each sample was subjected to observation under both thermal and plasma-assisted conditions, with each observation lasting 15 min and 20 min, respectively. A total of three observations were conducted for each condition. After each observation, the surface of the catalyst was purged with Ar and then regenerated with a mixture of Ar and CO2 to maintain its almost identical surface chemical composition. In Fig. S4, representative experiment cycle data recorded from QMS is displayed. The parameters used to evaluate the performance of the DRM process are as follows:

**Conversion:** The reactant conversion determines the fraction of reactants that undergo into reaction. The reactant conversion can be calculated as follows.

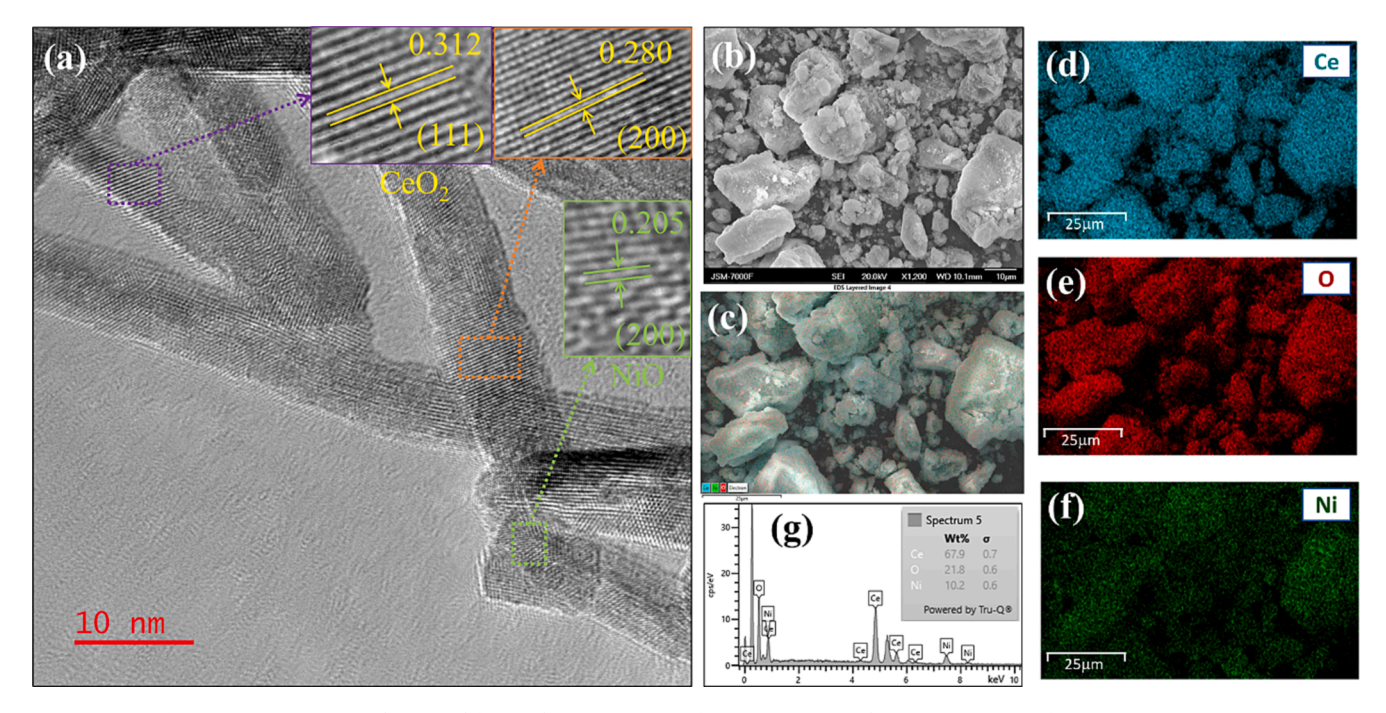


Fig. 5. (a) TEM image with exposed facets, (b) SEM image, (c-f) EDS mapping, and (g) EDS spectrum of 10 wt% Ni-CeO2 NR.

$$CH_{4} \, conversion = \left[\frac{moles \, of \, CH_{4} \, consumed}{moles \, of \, CH_{4} \, input}\right] \times 100\% \tag{2}$$

$$CO_{2} conversion = \left[\frac{moles of CO_{2} consumed}{moles of CO_{2} input}\right] \times 100\%$$
(3)

**Yield:** The yield of a particular reaction determines the reaction's efficiency. The yield can be determined using the ratio of the output product to the input reactants.

$$CO \text{ yield} = \left[\frac{\text{moles of CO produced}}{\text{moles of } (CH_4 + CO_2) \text{ input}}\right] \times 100\% \tag{4}$$

$$H_2 \text{ yield} = \left[ \frac{\text{moles of } H_2 \text{ produced}}{2 \times \text{moles of } CH_4 \text{ input}} \right] \times 100\%$$
 (5)

**Selectivity:** The percentage of unwanted products produced alongside intended products is determined by selectivity. This is calculated by comparing the produced products and the actual reactants used.

$$CO \, Selectivity = \left[\frac{moles \, of \, CO \, produced}{moles \, of \, (CH_4 + CO_2) \, consumed}\right] \times 100\% \tag{6}$$

$$H_2 \text{ selectivity} = \left[ \frac{\text{moles of } H_2 \text{ produced}}{2 \times \text{moles of } CH_4 \text{ consumed}} \right] \times 100\% \tag{7}$$

Carbon balance and  $H_2/CO$  ratio: The  $H_2/CO$  ratio provides a sense of the relative proportion of products, whereas the carbon balance determines the amounts of carbon in various formats.

$$H_2/CO = \left[\frac{\text{moles of } H_2 \text{ produced}}{\text{moles of CO produced}}\right] \tag{8}$$

$$\begin{aligned} \text{Carbon balance} &= \left[ \frac{\text{moles of } (\text{CO} + \text{CO}_2 + \text{CH}_4) + 2 \times \text{ moles of } \text{C}_2 \text{H}_6}{\text{moles of } \text{CH}_4 \text{ input} + \text{moles of } \text{CO}_2 \text{ input}} \right] \\ &\times 100\% \end{aligned}$$

Specific input energy (SIE) and Energy efficiency (EE): The SIE calculates the plasma energy necessary to process the input gas and correlates plasma power with the overall feed gas supplied. On the other

hand, another critical performance parameter, EE, shows how much feed gas is transformed while utilizing a unit amount energy.

$$SIE(kJ/L) = \left[ \frac{Input \, Power \left( W \right) \times 60}{Total \, Flow \, Rate \left( mL/min \right) \times 1000} \right] \tag{10}$$

$$EE\left(mmol/kJ\right) = \left[\frac{moles \ of \ (CH_4 + CO_2) \ consumed \ per \ minute \times 10^6}{Input \ Power \ (W) \times 60}\right] \tag{11}$$

# 3.2.1. Packing Material, Support, and catalyst performance

The thermal and plasma-assisted DRM performances were evaluated using three samples: quartz wool (as the packing material), CeO2 NR support, and 10 wt% Ni-CeO2 NR catalyst. The experiments were carried out at a constant temperature of 350 °C and plasma power of 23.8 W, aiming to investigate and compare the response of each sample in the catalytic process. The total volume flow rate was carefully regulated at 350 cm<sup>3</sup>/min, equivalent gas hourly space velocity (GHSV) of 3720 h<sup>-1</sup> and 16.1 ms residence time, while the CH4 to CO2 ratio was fixed at 100:250 (=0.4). Quartz wool and CeO2 NR support were inert for thermal DRM, but showed some progress in plasma-assisted catalysis. Fig. 6 provides a comparison of performance parameters, including conversion, yield, selectivity, carbon balance, H2/CO ratio, and C-2 hydrocarbon production, for the packing material, support, and catalyst in both thermal and plasma-assisted conditions. As depicted in Fig. 6(a), the CH<sub>4</sub> conversion in plasma-assisted DRM was consistently higher than the CO<sub>2</sub> conversion, regardless of the sample type used. In contrast, the CO<sub>2</sub> conversion was relatively higher in pure thermal DRM. This underscores the critical role played by the oxygen vacancy rich CeO<sub>2</sub> NR support in facilitating CO<sub>2</sub> activation (adsorption/dissociation) during thermal DRM, contributing to a bifunctional reaction mechanism. The introduction of plasma to the DRM reaction enhances CH4 dissociation and promotes its conversion over CO<sub>2</sub>, primarily due to the lower bond dissociation energy (BDE) of CH<sub>4</sub> (440 kJ/mol) compared to that of CO<sub>2</sub> (523 kJ/mol) [52]. The presence of a lower quantity of CH<sub>4</sub> relative to CO<sub>2</sub> in the supply may also contribute, as the plasma energy is adequate to break fewer CH<sub>4</sub> bonds. These additional reacted CH<sub>4</sub> in the presence of plasma compared to thermal DRM helped to produce other species along with H<sub>2</sub>, as indicated by the graphs of yield, selectivity, and C<sub>2</sub>H<sub>6</sub>

(9)

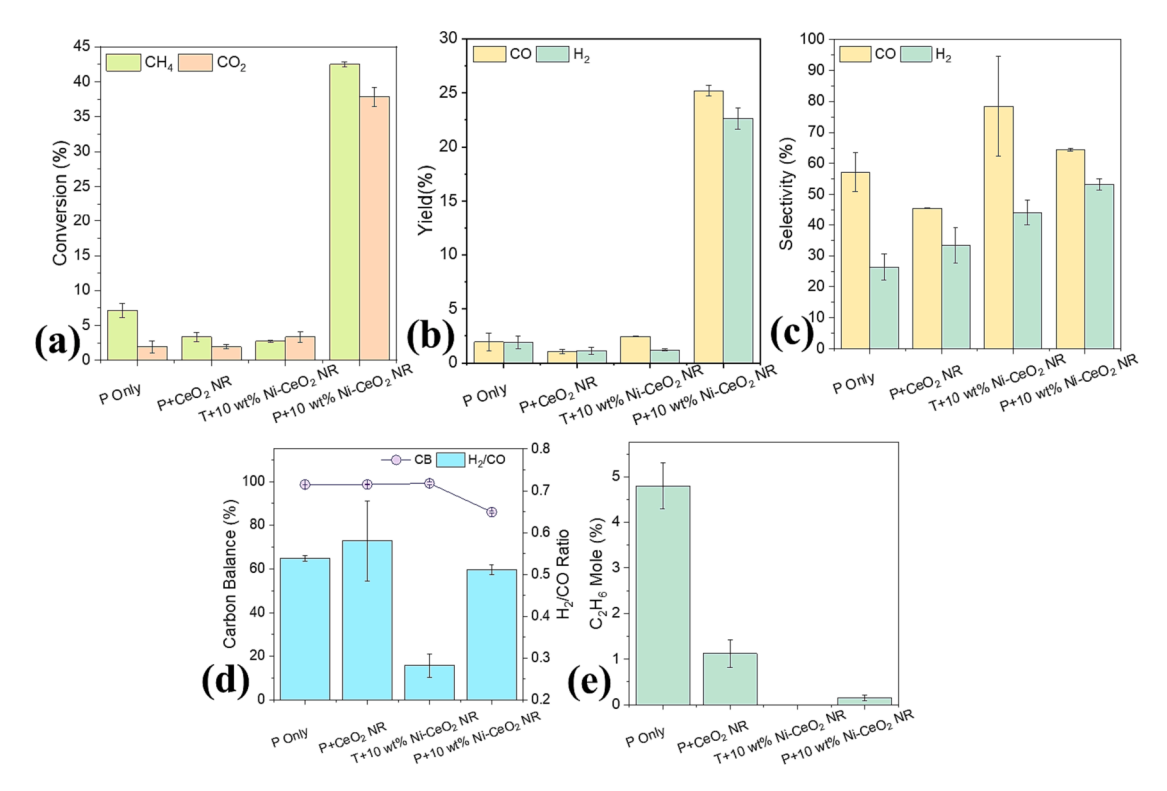


**Fig. 6.** (a) CH<sub>4</sub> and CO<sub>2</sub> conversion, (b) Yield, (c) Selectivity, (d) Carbon balance and H<sub>2</sub>/CO ratio, and (e) C<sub>2</sub>H<sub>6</sub> mole percentage for support and catalyst under plasma and thermal conditions, P: Plasma, T: Thermal (Furnace temperature: 350 °C, Plasma power: ~23.8 W, Feed gas (CH<sub>4</sub>:CO<sub>2</sub>): 100:250).

formation shown in Fig. 6(b), 6(c), and 6(e), respectively. When testing quartz wool alone, a notable quantity of C<sub>2</sub>H<sub>6</sub> was produced. However, the introduction of CeO2 NR or 10 wt% Ni-CeO2 NR into the reactor led to a noticeable decrease in C<sub>2</sub>H<sub>6</sub> production, indicating an inhibitory effect on C<sub>2</sub>H<sub>6</sub> formation. It is worth highlighting that among the tested samples, the 10 wt% Ni-CeO2 NR catalyst demonstrated the lowest level of C<sub>2</sub>H<sub>6</sub> production. It might be due to the gaseous C<sub>2</sub>H<sub>6</sub> being adsorbed on the Ni surface and splitting into  $\text{CH}_{3\ (ads)}$  at the active Ni sites in the ethane dissociation reaction (Eq. (12)) as described in the literature [53]. Another possibility is the ethane catalytic combustion reaction (Eqn. (13)), where the oxygen radicals (O') coming from CO<sub>2</sub> dissociation ( $CO_{2 \text{ (ads)}} \rightarrow CO_{\text{ (ads)}} + O'$ ) on the  $CeO_2$  surface react with surface adsorbed  $C_2H_6$  (ads) or  $CH_3$  (ads) and produce  $CO_2$  with  $H_2O$  [54]. This ethane catalytic reaction can also occur with adsorbed oxygen due to the oxygen vacancy in the CeO2 support. Enhanced CH4 and CO2 conversions observed in the 10 wt% Ni-CeO2 NR catalyst underscore the significant presence of enriched oxygen vacancy/exchange/diffusion. which is closely associated with the improved metal-support interaction. The role of oxygen vacancies in promoting CO<sub>2</sub> activation was investigated through a combination of DFT simulations [55], experimental studies [56] previously. Plasma coupling in combination with oxygen vacancy effect contributing to the improved catalytic performance.

$$C_2H_{6(g)} \to C_2H_{6(ads)} \to CH_{3(ads)}$$
 (12)

$$C_2H_{6(g)} \rightarrow C_2H_{6(ads)} + O' \rightarrow CO_{2(g)} + H_2O_{(g)}$$
 (13)

The integration of plasma-thermal-catalyst synergy resulted in the highest performance in terms of conversion, yield, selectivity, and  $\rm H_2/CO$  ratio compared to both pure thermal-catalytic and plasma-only conditions. In case of pure thermal DRM, only a small amount of reaction was observed when the 10 wt% Ni-CeO $_2$  NR catalyst was tested. In contrast, the conversions in plasma-assisted DRM for the same catalyst were substantially higher. The 10 wt% Ni-CeO $_2$  NR catalyst in plasma-assisted DRM achieved greater CH $_4$  and CO $_2$  conversions than the pure thermal environment, but there was a decrease in CO output and an

increase in H<sub>2</sub> generation, as indicated in the selectivity plot in Fig. 6(c). The reason might be that the presence of water vapor facilitates the water gas shift (WGS) reaction, which is desirable at lower temperatures (<800 °C), leading to the formation of H<sub>2</sub> and the reduction of CO [57,58]. An additional factor could be the deposition of carbon rather than the formation of CO where CH<sub>x</sub> (x=1-3) could go through splitting into coke on the catalyst surface. The carbon deposition rate was determined through a carbon balance calculation, as illustrated in Fig. 6 (d), and it was observed that the 10 wt% Ni-CeO<sub>2</sub> NR catalyst exhibited the highest deposition rate. The presence of C<sub>2</sub>H<sub>6</sub> in the case of quartz wool or CeO<sub>2</sub> NR support prevented carbon deposition on the surface, resulting in minimal unbalanced carbon accumulation. At a lower temperature, such as 350 °C, in a pure thermal environment, the Ni catalyst exhibited lower thermal activity, leading to a reduced conversion rate and consequently, less carbon deposition. In contrast, in the presence of plasma at the same temperature, the Ni catalyst became more active, as described by other researcher [21], facilitating the breaking of the  $C_2H_6$  species bond through ethane cracking (Eqn. (15)). Simultaneously, the possibility of additional reactions such as the Boudouard reaction (Eqn. (18)), methane cracking (Eqn. (16)), and steam generation (Eqn. (17)) escalated, contributing to the deposition of additional carbon. Therefore, the best performance was achieved for the 10 wt% Ni-CeO2 NR catalyst in the plasma-catalyst synergistic DRM reaction under fixed conditions, including plasma power, temperature, flow rate, and flow ratio, as depicted in the various performance graphs.

WGS Reaction : 
$$CO_{(g)} + H_2O_{(g)} = CO_{2(g)} + H_{2(g)} (\Delta H_{298K}$$
  
=  $-41.2 \, kJ \, mol^{-1})$  (14)

$$\mbox{Ethane Cracking}: \ C_{2}H_{6\,(g)} = 2C_{\,(s)} + 3H_{2\,(g)}, \quad \ C_{2}H_{6\,(s)} + H_{2\,(g)} = 2CH_{4\,(g)} \eqno(15)$$

$$\mbox{Methane Cracking}: \mbox{ } CH_{4\,(g)} = C_{\,(g)} + 2H_{2\,(g)} \ \ \, (\Delta H_{298K} = +75 \mbox{ kJ mol}^{-1}) \label{eq:H298K}$$

Steam Generation : 
$$CO_{2 (g)} + 2H_{2 (g)} = C_{(s)} + 2H_{2}O_{(g)} (\Delta H_{298K}$$
  
=  $-90 \text{ kJ mol}^{-1})$  (17)

Boulouard Reaction : 
$$2CO_{(g)} = C_{(s)} + CO_{2(g)} (\Delta H_{298K}$$
  
=  $-172.4 \text{ kJ mol}^{-1})$  (18)

#### 3.2.2. Thermal effect

The temperature dependency of thermal and plasma-assisted catalytic DRM is depicted in Fig. 7(a)-(e) for a constant flow condition (CH<sub>4</sub>:  $CO_2 = 100:250$ ). Plasma power, ranging from 22.5 to 25.5 W, was applied along with temperatures spanning 100 to 450 °C, as shown in Fig. S1(b). The CH<sub>4</sub> and CO<sub>2</sub> conversions for both the CeO<sub>2</sub> NR support and the 10 wt% Ni-CeO2 NR catalyst under both plasma-assisted and pure thermal conditions are depicted in Fig. 7(a) and 7(b) respectively. The performance improved with rising temperature in all scenarios, although the rate of improvement varied based on the catalyst-support interaction and reaction kinetics. Initially, the conversions for CeO2 NR support alone in plasma-assisted DRM displayed a slight rise until 250 °C, after which it became almost constant. The highest CH<sub>4</sub> and CO<sub>2</sub> conversions were observed around 4.0 % and 2.3 %, respectively, at a maximum temperature of 450 °C. In contrast, for 10 wt% Ni-CeO2 NR both conversions increased with temperature under both pure thermal and plasma-assisted synergy conditions, with the highest conversions. For pure thermal DRM, catalyst reactivity was not observed until temperatures reached 350 °C, whereas plasma-assisted catalytic activity was initiated at very low temperatures, such as 100 °C. Under pure thermal conditions, NiO reduction occurs at approximately 300 °C, as observed in the TPR analysis, providing confirmation of the NiO activation temperature for thermal DRM. Upon introducing plasma to the system at 350 °C, the CH<sub>4</sub> and CO<sub>2</sub> conversions experienced a substantial increase of 40 % and 34 %, respectively. The difference between conversion data of plasma-thermal synergy and pure thermal conditions at each

temperature, as depicted in the figure, indicates that plasma exhibits the most significant and suitable contribution at 350 °C, followed by 400 °C and 450 °C. At 450 °C, this catalyst achieved a maximum CH<sub>4</sub> and CO<sub>2</sub> conversion of 52.1 % and 46.1 %, respectively. If plasma was not utilized, a temperature of more than 750 °C was required to obtain the same conversion amount for irregularly shaped Ni-CeO<sub>2</sub> [59].

The conversion results provided evidence to conclude that the 10 wt % Ni-CeO<sub>2</sub> NR catalyst exhibited higher activity in a plasma-assisted environment compared to its pure thermal environment or the CeO<sub>2</sub> NR support alone in a plasma-assisted environment. The additional performance parameters, including yield, selectivity, hydrogen to carbon monoxide (H<sub>2</sub>/CO) ratio, carbon balance, and energy efficiency (EE) with temperature variations are presented in Fig. 7(c)-(e) specifically for the 10 wt% Ni-CeO<sub>2</sub> NR catalyst under plasma-assisted conditions. Both CO and H<sub>2</sub> yields exhibited an increase with temperature, although the CO yield surpassed the H<sub>2</sub> yield up to 400 °C, after which the H<sub>2</sub> yield became higher, as illustrated in Fig. S1(a). This trend was also evident in the selectivity data, where H<sub>2</sub> selectivity initially experienced a gradual decline, but began to rise after reaching 350 °C. This shift in selectivity can potentially be attributed to the growing influence of thermal catalysis, which becomes dominant at temperatures around 350 °C, as indicated by the conversion data. The effects of thermal catalysis prompt a higher production of H2 and a relatively lower production of CO, likely due to changes in the desorption behavior of the catalyst surface. Beyond 350 °C, the WGS reaction (Eq. (14)) is likely facilitated by the combined effects of thermal catalysis and plasma, leading to an enhanced rate of H2 production and a reduction in CO production. Consequently, the selectivity data aligned with this trend. The increased H<sub>2</sub> production ultimately contributed to an elevated H<sub>2</sub>/ CO ratio, as depicted in Fig. 7(d), reaching its peak value of approximately 0.62 at 450 °C.

Furthermore, data on  $C_2H_6$  selectivity show that plasma catalysis is most effective in producing C-2 hydrocarbon at low temperatures. With

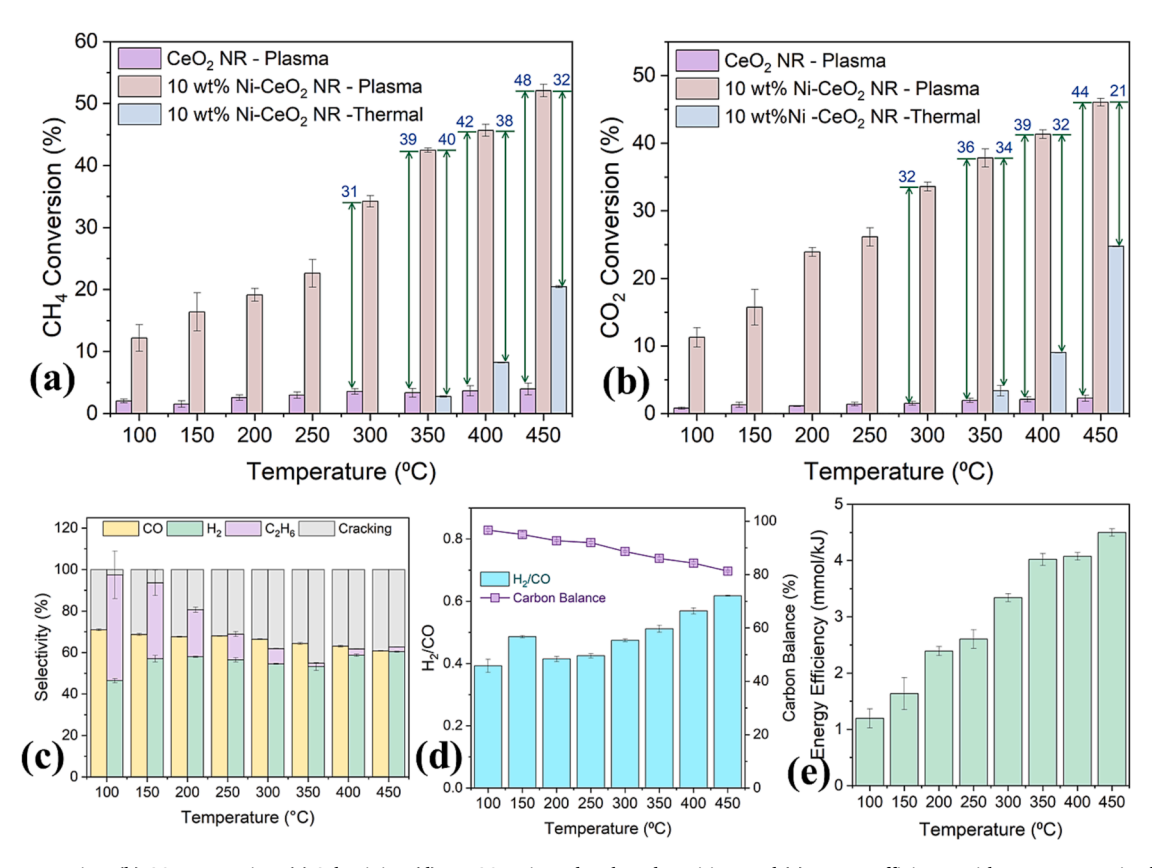


Fig. 7. (a) CH<sub>4</sub> conversion, (b) CO<sub>2</sub> conversion, (c) Selectivity, (d) H<sub>2</sub>/CO ratio and carbon deposition, and (e) Energy efficiency with temperature rise for 10 wt% Ni-CeO<sub>2</sub> NR (Plasma power: 22.5–25.5 W, Feed gas (CH<sub>4</sub>:CO<sub>2</sub>): 100:250).

the temperature increase, the higher activity of the Ni catalyst promotes the decomposition of C<sub>2</sub>H<sub>6</sub> and the generation of other species through ethane cracking (Eq. (15)) and ethane dry reforming (Eq. (19)) reactions. The carbon balance plot in Fig. 7(d) illustrates the increasing rate of carbon deposition as the temperature rises. As the temperature increased, a greater number of active sites on the Ni were activated, which enhanced the possibility of methane cracking (Eqn. (16)) and the Boudouard reaction (Eq. (18)), which ultimately enhanced carbon coking. Considering that the plasma power remained relatively constant, the EE followed a comparable trend to the conversion as shown in Fig. 7(e). At a temperature of 450 °C, the maximum EE achieved was 4.5 mmol/kJ. The shape effect made the 10 wt% Ni-CeO2 NR catalyst more catalytically active as temperature rises, particularly in the presence of plasma interactions. However, this increased activity was accompanied by elevated carbon deposition, ultimately leading to catalyst deactivation, similar to the behavior observed in irregularly shaped Ni-CeO2 catalysts [59].

$$C_2H_{6(g)} + 2CO_{2(g)} = 4CO_{(g)} + 3H_{2(g)} \quad (\Delta H_{298K} = +428.1 \text{ kJ mol}^{-1})$$
 (19)

#### 3.2.3. Plasma power effect

The plasma power effect in the form of SIE on DRM performance for 10 wt% Ni-CeO2 NR was investigated at 350 °C, where the plasma voltage (11.8 kV) and flow condition (CH<sub>4</sub>:CO<sub>2</sub> = 100:250) remained fixed. As the size of the reactor remains constant, the SIE is directly proportional to the plasma power. The conversion, selectivity, carbon balance, H<sub>2</sub>/CO ratio, and energy efficiency trends are shown in Fig. 8 (a)-(d) when plasma power was varied by changing the applied current by adjusting the plasma driver's duty cycle. As shown in Fig. 8(a), increasing SIE from 1.42 to 4.65 kJ/L increased CH<sub>4</sub> and CO<sub>2</sub> conversion from 25.5 % to 57.8 % and from 20.0 % to 39.1 %, respectively. Because, an escalation in plasma power enables the breakdown of a larger quantity of reactant gas, thereby leading to an enhancement in conversion. As the energy was applied up to 3.96 kJ/L, the CO selectivity reduced, and the H2 selectivity rose, but as energy increased further, the CO selectivity rose, and the H2 selectivity fell. So the behavior of increasing conversions and decreasing selectivity above the plasma power of 3.96 kJ/L demonstrated the involvement of reactants to produce other species besides H<sub>2</sub> and CO. The H<sub>2</sub>/CO ratio also supported the trend by being greater at 3.96 kJ/L and lesser at 4.65 kJ/L since the H<sub>2</sub> production decreased at 4.65 kJ/L. The most likely explanation in a broader sense is the dominance of the WGS reaction up to 3.66 kJ/L of applied SIE, whereas the reverse water gas shift (RWGS) (Eq. (20)) reaction's dominance extends beyond 3.66 kJ/L of applied SIE. The RWGS reaction is usually favorable at high temperatures (>800 °C), and this result suggests it may be effective at high plasma power even at lower temperatures.

The amount of carbon deposited increased with applied SIE, with the maximum carbon deposition occurring at the highest SIE. Because high plasma power might easily dissociate CH<sub>4</sub> and CO<sub>2</sub> at the elementary

level and eventually lead to methane cracking (Eq. (16)) and the Boudouard reaction (Eq. (18)). As seen in Fig. 8(d), as the input energy of the plasma increased, the plasma energy efficiency decreased. Consequently, operating at a lower plasma power is advantageous regarding energy efficiency, but this results in ineffective conversions. For this particularly nanorod shaped catalyst, increased plasma power diverted the reaction away from DRM, which finally caused the catalyst to deactivate quickly. In contrast, optimally applied power could pave the way for DRM.

$$RWGS: \ CO_{2\,(g)} + H_{2\,(g)} = CO_{\,(g)} + H_{2}O_{\,(g)} \left(\Delta H_{298K} = +41.2\,\text{kJ mol}^{-1}\right) \eqno(20)$$

#### 3.2.4. Fluid flow effect

The proportion and flow of reactants may affect the reaction's kinetics, which may modify how the catalyst and support interact to produce the intended quantity of products. So, this investigation looked at how fluid parameters influenced DRM performance. Fig. 9(a)-(c) illustrates the reactant conversion, product selectivity, carbon balance, and the  $H_2/CO$  ratio for a range of feed gas flow ratios tested at 350 °C temperature while maintaining a constant total flow of 350 cm<sup>3</sup>/min (equivalent GHSV of 3720  $h^{-1}$ ), plasma power of around 23.8 W, and applied voltage of 11.8 kV. The findings showed that CH<sub>4</sub> and CO<sub>2</sub> conversion decreased as the CH<sub>4</sub>:CO<sub>2</sub> ratio increased (i.e., as the CH<sub>4</sub> amount rose) until they hit a critical ratio ( $CH_4:CO_2 = 175:175 = 1$ ), at which time they started to rise. Numerous factors could influence the reaction kinetics as both conversions decreased with the flow ratio. One explanation is that the reactions are mass transfer controlled, whereby a sufficient number of radicals may be created in gaseous phases but cannot reach the surface at a specific proportion due to mass transfer limitation, hence reducing the reaction rate. According to the selectivity plot, the CO selectivity grew until  $CH_4:CO_2 = 1$  and then declined, while the H<sub>2</sub> selectivity progressively dropped as the ratio rose and nearly remained constant after  $CH_4:CO_2 = 1$ . The gradual decrease in  $H_2$  production, regardless of conversion rate, may be caused by the involvement of H2 in other reactions. Two possible reactions are steam generation (Eq. (17)) and RWGS (Eq. (20)), where H2 converts into H2O in both cases. The RWGS route could also be responsible for CO production, with CO production increasing until  $CH_4$ : $CO_2 = 1$ . When  $CH_4$ : CO<sub>2</sub> > 1, preferring steam generation over RWGS decreases CO output and increases CO<sub>2</sub> conversion. The carbon balance in Fig. 9(c) exhibited the CO selectivity's reverse tendency, with a maximum value at a CH<sub>4</sub>:  $CO_2 = 1$  and a steadily falling before and after this ratio. As the conversion was also lower at CH<sub>4</sub>:CO<sub>2</sub> = 1, the amount of carbon released was likewise at its lowest because the probability of coke formation reactions decreased. On the other hand, the likelihood of coke formation was higher with relatively higher conversion rates. The implications determine which feed gas ratio for DRM is most advantageous. For instance, if a larger H2/CO ratio is required, a feed gas ratio greater than unity may be utilized, whereas unity is favored for lower carbon

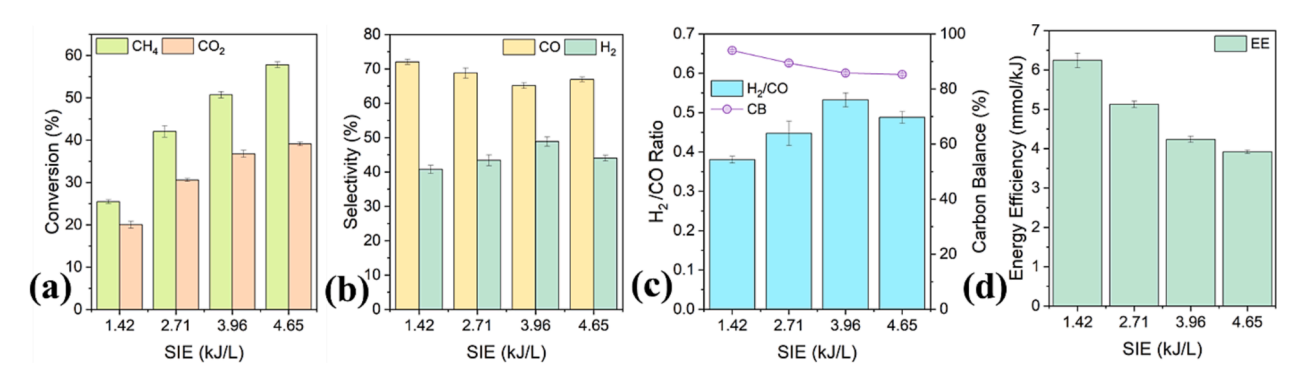


Fig. 8. (a) Conversion (b) Selectivity (c) H<sub>2</sub>/CO ratio and carbon balance (d) Energy efficiency of 10 wt% Ni-CeO<sub>2</sub> NR under different plasma power in the form of SIE (Furnace temperature: 350 °C, Feed gas (CH<sub>4</sub>:CO<sub>2</sub>): 100:250).

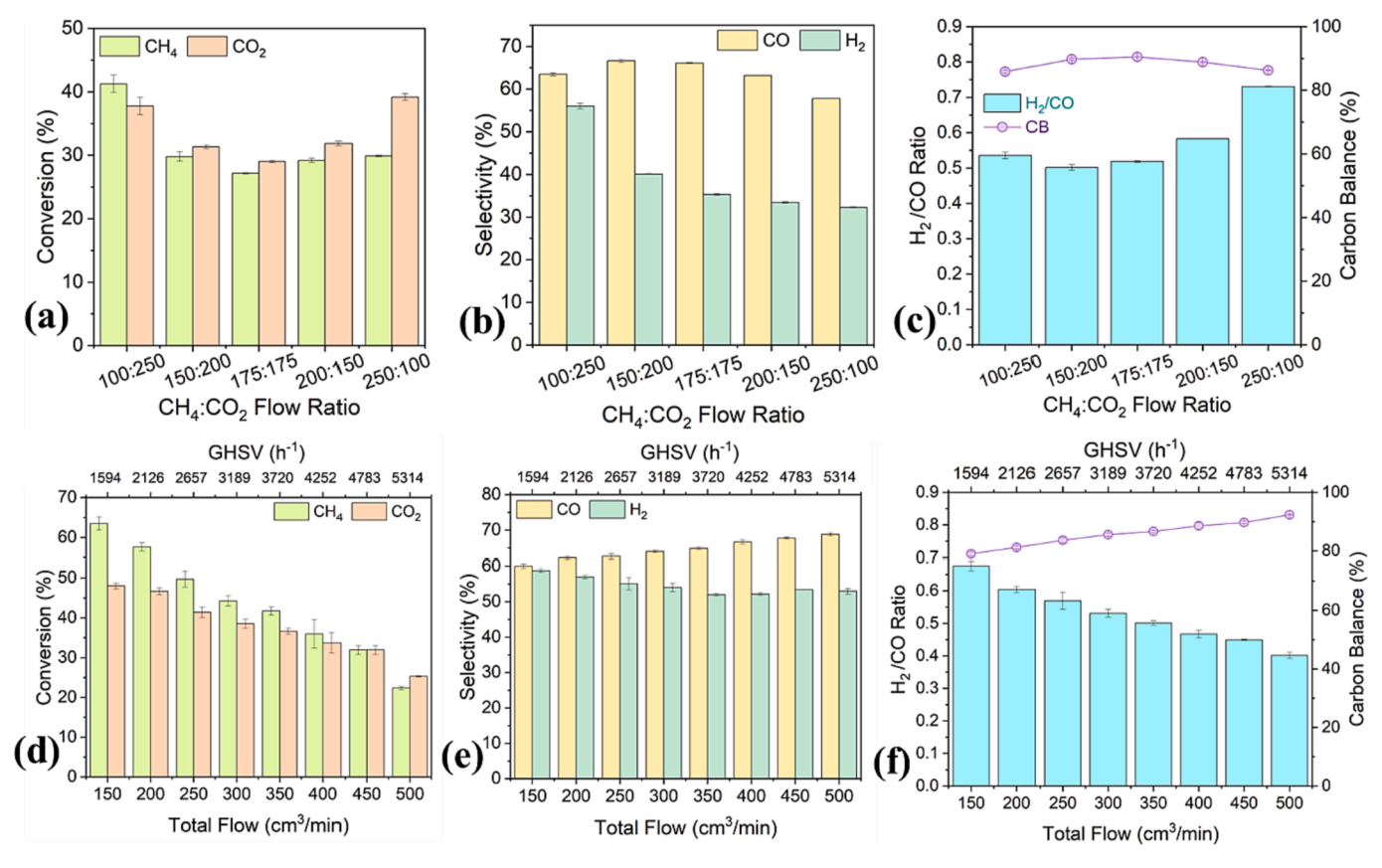


Fig. 9. (a, d) Conversion, (b, e) Selectivity, and (c, f) H<sub>2</sub>/CO ratio and carbon balance of 10 wt% Ni-CeO<sub>2</sub> NR at different flow ratios and total flow (Furnace temperature: 350 °C, Plasma power: ~23.8 W).

deposition. In terms of energy efficiency, as illustrated in Fig. S3(a), the optimal energy-efficient flow ratio is 0.4 for a fixed total flow rate of  $350~\text{cm}^3/\text{min}$ .

The impact of total flow was also examined at 350 °C, where the plasma power of around 23.8 W, applied voltage of 11.8 kV, and flow ratio of  $CH_4:CO_2 = 0.4$  were constants. The performance parameters associated with total flow rate are illustrated in Fig. 9(d)-(f), where maximum CH<sub>4</sub> and CO<sub>2</sub> conversion was found at lower flow rates, in this instance 150 cm<sup>3</sup>/min (equivalent GHSV of 1594 h<sup>-1</sup>). The performance improves because less gas is delivered at a lower flow rate, and reactants have more time to dwell in the reaction zone. Higher flow rates ensure more feed gas supply, resulting in shorter chemical residence times that divert in the opposite direction. Fig. S2(b) depicts the chemical residence time and flow rate relationship. The selectivity plot in Fig. 9(e) depicts the rising CO and falling H2 trends. One possibility is the dominance of the RWGS reaction (Eq. (20)) with an increasing overall flow rate. The H<sub>2</sub>/CO ratio decreased as the total flow increased, which is more significant because higher flow rates resulted in less H2 generation because of RWGS dominance. The conversion and carbon deposition decreased as the overall flow rose, peaking at the lowest flow rate. The reactants had more time to participate in reactions when the total flow rate was lower; consequently, conversions were higher. As a result, the maximum EE is found at lower flow rates because it is more closely related to feed gas transformed at a fixed plasma power. Fig. S2(a) illustrates how the applied power and EE vary with the total flow. Even though conversion and EE are higher at a lower total flow rate, the required product selectivity could not reach a significant value since slow reactions were focused and altered the reaction's path. However, DRM reaction came into focus at higher total flow rates, although relative product formation reduced. Considering other performance data, the 300-350 cm<sup>3</sup>/min total flow range is suitable for DRM operation at a fixed feed gas ratio of 0.4. for this nanorod shaped catalyst.

## 3.3. Comparative performance assessment

In the plasma-assisted DRM process, multiple elementary reactions take place at the surface and radical levels. The predominance of global reactions differs based on the specific reaction parameters. Table 2 provides an overview of the primary side reaction (excluding carbon cracking reaction) that dominates the overall process for the 10 wt% Ni-CeO $_2$  NR catalyst of the specified shape.

#### 3.4. Spent catalyst inspection

Plasma DRM delivered better conversion than thermal DRM, but it also produced much more carbon in the deposited form, which was determined from previous investigations under different reaction conditions. Table 2 summarized the maximum and minimum carbon deposition conditions for various reaction environments. As the temperature increased, the Ni catalyst inhibited the generation of C-2 hydrocarbon and deposited carbon, as was previously observed. The analysis of the used catalyst examined the verification of carbon in deposited forms. Fig. 10(a) depicts the calculated unbalanced carbon during plasma-assisted and pure thermal catalysis with temperature rise, where most carbon was found in the deposited form. The spent catalysts were characterized using the XRD, SEM, and EDX techniques after 6 h of testing in pure thermal and plasma-assisted conditions at 450 °C to examine the carbon deposition on the catalyst surface. After thermal DRM, the spent catalyst XRD pattern in Fig. 10(b) did not exhibit any carbon peak, but after plasma DRM, the spent catalyst showed prominent  $2\theta$  peaks of graphite at  $26.6^{\circ}$ ,  $42.4^{\circ}$ , and  $44.6^{\circ}$ . Additionally, two more peaks were found at 44.5° and 51.9°, which were associated with the metal Ni because some NiO was converted to Ni in the presence of H<sub>2</sub> in the plasma-assisted environment. Compared to plasma-assisted DRM, less carbon was deposited during thermal DRM; therefore, the XRD

**Table 2**Maximum performance, carbon deposition, and dominated side reactions under different reaction environments.

different reaction cuvironments.					
Reaction Environment	Overall Dominated Side Reaction	Maximum Performance	Carbon Deposition Condition		
Thermal Effect Plasma Power: 22.5—25.5 W  Temperature: 100–450 °C Feed Gas Flow & ratio:	WGS reaction (Eqn. (14))	$CH_4 = 52.1$ % and $CO_2 = 46.1$ % conversion at $450$ °C EE = $4.5$ mmol/kJ at $450$ °C $H_2/CO = 0.62$ at	Highest at 450 and lowest at 100 °C		
350 cm <sup>3</sup> /min,		450 °C			
0.4 <u>Plasma Power</u> <u>Effect</u>	WGS reaction (Eqn. (14)) from 8.3 to	$CH_4 = 57.8 \%$ and $CO_2 = 39.1 \%$	Highest at 27.1 and lowest at		
Plasma Power: 8.3–27.1 W	23 W and RWGS reaction (Eqn.	conversion at 27.1 W	8.3 W		
Temperature: 350 °C Feed Gas Flow & ratio: 350 cm <sup>3</sup> /	(20)) from 23 to 27.1 W	EE = 6.3 mmol/kJ at 8.3 W H <sub>2</sub> /CO = 0.53 at 23 W			
min, 0.4 Feed Gas Ratio	RWGS reaction	$CH_4 = 41.2 \%$	Highest at 0.4		
Effect Plasma Power: 23.8 W Temperature: 350 °C Feed Gas Flow & ratio: 350 cm <sup>3</sup> /	(Eqn. (20)) from 0.4 to 1 and steam generation reaction (Eqn. (17)) from 1 to 2.5	conversion at 0.4 and $CO_2 = 39.2$ % conversion at 2.5 EE = 3.9 mmol/kJ at 0.4 $H_2/CO = 0.73$ at 2.5	and lowest at 1		
min, 0.4-2.5					
Feed Gas Flow Effect Plasma Power:	RWGS reaction (Eqn. (20))	$CH_4 = 63.5 \%$ and $CO_2 = 48 \%$ conversion at 150	Highest at 150 cm <sup>3</sup> /min and lowest at 500		
23.8 W Temperature: 350 °C		$cm^3/min$ EE = 5.4  mmol/kJ at 150 cm <sup>3</sup> /min	cm <sup>3</sup> /min		
Feed Gas Flow & ratio: 100–500 cm <sup>3</sup> /min, 0.4		$H2/CO = 0.68 \text{ at}$ $150 \text{ cm}^3/\text{min}$			

pattern did not show a carbon peak, which complied with the carbon balance calculation. The SEM micrographs in Fig. 11(a-c) exhibit carbon on the surfaces of the used catalysts in both nanotube and particle form. The EDS spectrum confirmed the elemental composition in Fig. 11(i), and the EDS mapping in Fig. 11(d-h) illustrated the distribution of

carbon across the catalyst surface. The deposited carbon weight percentage was not uniform on all catalyst particles' surfaces. The catalyst surface was blocked by the structured carbon that was typically in nanotube form, preventing reactants from reacting with the catalyst, which results in deactivation even for this shaped catalyst.

#### 4. Conclusion

This study focused on conducting DRM in a DBD plasma reactor to investigate the impact of plasma on a nanostructured Ni catalyst supported on CeO2 NR. The effects of plasma addition were examined by comparing the catalyst's performance in both thermal and plasmaassisted synergistic conditions while also evaluating the DRM activity of CeO2 NR support and a catalyst-free system (utilizing only quartz wool). The results revealed that the addition of plasma to the thermal DRM process significantly enhanced CH<sub>4</sub> conversion more than CO<sub>2</sub> conversion, and plasma contribution to conversions is greatest at 350 °C. Increasing the temperature accelerated the conversion process, simplifying the carbon deposition pathway. Notably, the influence of plasma power dominance was explored at a fixed temperature of 350 °C and flow conditions ( $CH_4:CO_2 = 100:250$ ). It was observed that higher plasma power levels could enhance conversions, but beyond a certain threshold, excessive carbon deposition occurred, resulting in a lower H<sub>2</sub>/CO ratio. However, the process is more energy efficient at lower plasma input power.

Furthermore, the effect of reactant composition in the feed gas was examined at a constant temperature of 350 °C, a feed flow rate of 350 cm<sup>3</sup>/min, and a plasma power of approximately 23.8 W. Initially, both CH<sub>4</sub> and CO<sub>2</sub> conversions exhibited a declining trend until the mole ratios of CH<sub>4</sub> and CO<sub>2</sub> reached unity. Subsequently, as the CH<sub>4</sub>:CO<sub>2</sub> mole ratio increased beyond unity, the conversions showed an upward trend. The reaction demonstrated optimal energy efficiency at a mole ratio of 0.4. The total gas flow rate and residence time were found to have a strong correlation with the observed effects. Longer residence times led to more pronounced side reactions, resulting in extensive carbon deposition and higher H<sub>2</sub>/CO ratios. The DRM reaction kinetics were influenced by flow variables such as the feed gas mixture and flow rate, potentially leading to mass transfer or reaction-limited conditions. After 6 h of plasma-assisted DRM operation, the characterization of the spent catalyst revealed the formation of carbon nanotubes on the catalyst surface. This structured carbon deposition hindered surface accessibility and concurrently reduced catalytic activity. Additionally, the reduction of NiO to Ni resulted in a decrease in the number of active sites.

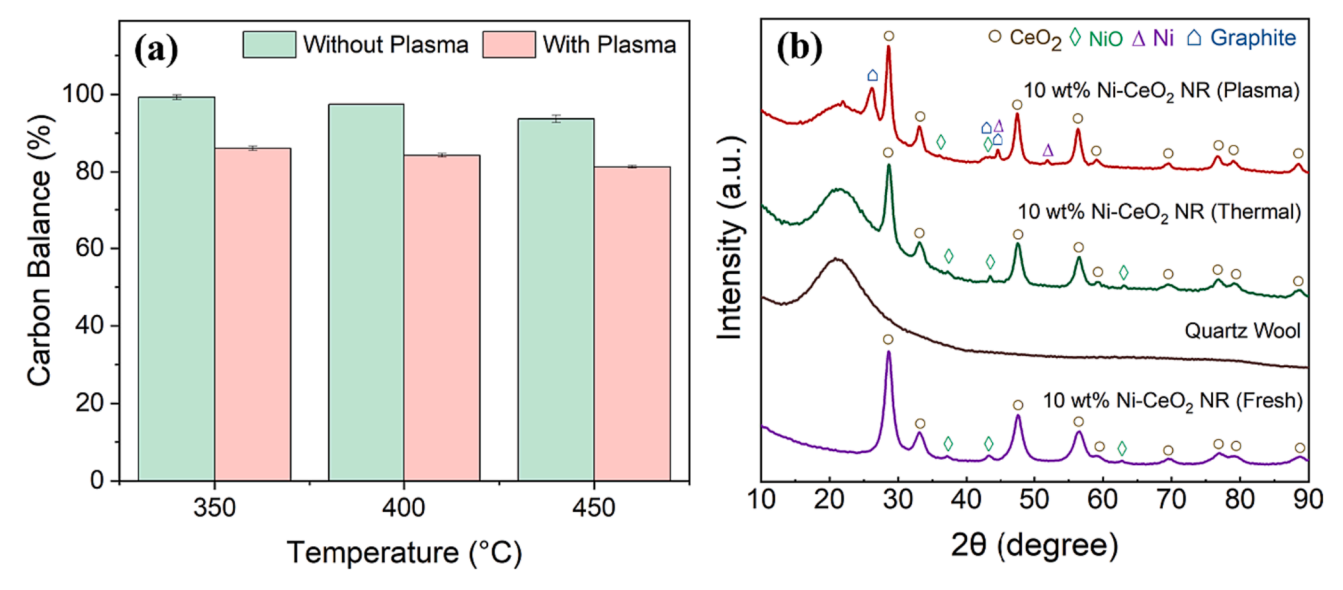


Fig. 10. (a) Carbon balance and (b) XRD pattern of fresh and used 10 wt% Ni-CeO<sub>2</sub> NR catalyst.

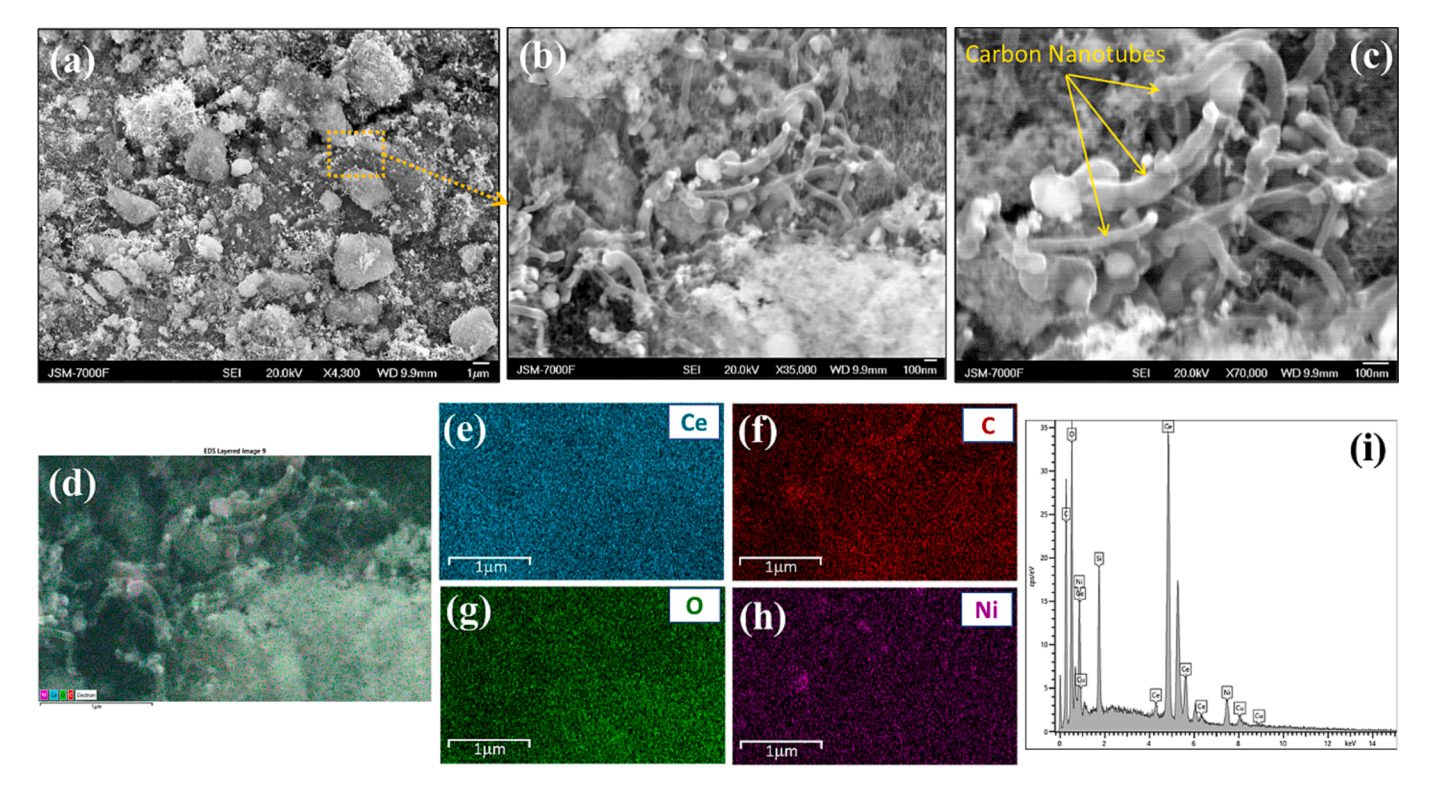


Fig. 11. (a-c) SEM images, (d-h) EDS elemental mapping, and (i) EDS spectrum of used 10 wt% Ni-CeO2 NR catalyst.

In conclusion, the nanorod-shaped catalyst exhibits enhanced MSI due to larger specific surface area and oxygen vacancy. The catalyst performs effectively under plasma-assisted conditions at lower temperatures pointing the capability plasma coupling with the catalyst. The reaction becomes energy-efficient based on the applied plasma power under specific reaction conditions, it becomes impractical in the long run due to substantial carbon deposition. These findings contribute to encourage a modest grasp of the complex interplay between plasma and shaped catalyst behavior in DRM systems.

# Declaration of competing interest

The authors declare that they have no known competing financial interests or personal relationships that could have appeared to influence the work reported in this paper.

#### Data availability

No data was used for the research described in the article.

# Acknowledgments

This work is supported by the National Science Foundation (1856729 and 2044733) and the use of SEM, TEM facilities at the Alabama Analytical Research Center (AARC) at The University of Alabama is gratefully acknowledged.

# Appendix A. Supplementary data

Supplementary data to this article can be found online at https://doi. org/10.1016/j.cej.2023.147459.

#### References

Statistical Review of World Energy | Energy economics | Home, (n.d.). https://www.bp.com/en/global/corporate/energy-economics/statistical-review-of-world-energy.html (accessed April 9, 2023).

- [2] Global Greenhouse Gas Emissions Data | US EPA, (n.d.). https://www.epa.gov/gh gemissions/global-greenhouse-gas-emissions-data (accessed April 4, 2023).
- [3] Two degrees of separation: ambition and reality, (n.d.). https://studylib.net/doc/18570122/two-degrees-of-separation-ambition-and-reality (accessed October 10, 2022).
- [4] R. Babakouhi, S.M. Alavi, M. Rezaei, E. Akbari, M. Varbar, Combined CO2 reforming and partial oxidation of methane over mesoporous nanostructured Ni/ M-Al2O3 catalyst: Effect of various support promoters and nickel loadings, J. CO2 Util. 70 (2023), 102427.
- [5] S. Fazlikeshteli, X. Vendrell, J. Llorca, Bimetallic Ru–Pd supported on CeO2 for the catalytic partial oxidation of methane into syngas, Fuel 334 (2023), 126799.
- [6] L. Li, N.H. Md Dostagir, A. Shrotri, A. Fukuoka, H. Kobayashi, Partial oxidation of methane to syngas via formate intermediate found for a ruthenium-rhenium bimetallic catalyst, ACS Catal. 11 (2021) 3782–3789.
- [7] M.I. Malik, I.E. Achouri, N. Abatzoglou, F. Gitzhofer, Intensified performance of methane dry reforming based on non-thermal plasma technology: Recent progress and key challenges, Fuel Process. Technol. 245 (2023), 107748.
- [8] S. Saeedi, X.T. Nguyen, F. Bossola, C. Evangelisti, V. Dal Santo, Methane Reforming Processes: Advances on Mono- and Bimetallic Ni-Based Catalysts Supported on Mg-Al Mixed Oxides, Catalysts 2023, Vol. 13, Page 379. 13 (2023) 379.
- [9] Z. Alipour, V. Babu Borugadda, H. Wang, A.K. Dalai, Syngas production through dry reforming: A review on catalysts and their materials, preparation methods and reactor type, Chem. Eng. J. 452 (2023), 139416.
- [10] M.A. Nieva, M.M. Villaverde, A. Monzón, T.F. Garetto, A.J. Marchi, Steam-methane reforming at low temperature on nickel-based catalysts, Chem. Eng. J. 235 (2014) 158–166.
- [11] A. Di Giuliano, K. Gallucci, Sorption enhanced steam methane reforming based on nickel and calcium looping: a review, Chem. Eng. Process. - Process Intesif. 130 (2018) 240–252.
- [12] S. Wang, S.A. Nabavi, P.T. Clough, A review on bi/polymetallic catalysts for steam methane reforming, Int. J. Hydrogen Energy 48 (2023) 15879–15893.
- [13] H. Schulz, Short history and present trends of Fischer-Tropsch synthesis, Appl. Catal. A 186 (1999) 3–12.
- [14] W.J. Jang, J.O. Shim, H.M. Kim, S.Y. Yoo, H.S. Roh, A review on dry reforming of methane in aspect of catalytic properties, Catal. Today 324 (2019) 15–26.
- [15] R. Snoeckx, A. Bogaerts, Plasma technology-a novel solution for CO2 conversion? Chem. Soc. Rev. 46 (2017) 5805–5863.
- [16] R. Snoeckx, Y.X. Zeng, X. Tu, A. Bogaerts, Plasma-based dry reforming: improving the conversion and energy efficiency in a dielectric barrier discharge, RSC Adv. 5 (2015) 29799–29808.
- [17] M.I. Boulos, P.L. Fauchais, E. Pfender, The Plasma State, Handbook of Thermal Plasmas. (2016) 1–53.
- [18] T. Paulmier, L. Fulcheri, Use of non-thermal plasma for hydrocarbon reforming, Chem. Eng. J. 106 (2005) 59–71.
- [19] E.C. Neyts, K. Ostrikov, M.K. Sunkara, A. Bogaerts, Plasma catalysis: synergistic effects at the nanoscale, Chem. Rev. 115 (2015) 13408–13446.

- [20] A.H. Khoja, M. Tahir, N.A.S. Amin, Recent developments in non-thermal catalytic DBD plasma reactor for dry reforming of methane, Energy Convers Manag. 183 (2019) 529–560.
- [21] X. Gao, Z. Lin, T. Li, L. Huang, J. Zhang, S. Askari, N. Dewangan, A. Jangam, S. Kawi, Recent Developments in Dielectric Barrier Discharge Plasma-Assisted Catalytic Dry Reforming of Methane over Ni-Based Catalysts, Catalysts 2021, Vol. 11, Page 455. 11 (2021) 455.
- [22] X. Tu, H.J. Gallon, M.V. Twigg, P.A. Gorry, J.C. Whitehead, Dry reforming of methane over a Ni/Al2O3 catalyst in a coaxial dielectric barrier discharge reactor, J. Phys. D Appl. Phys. 44 (2011), 274007.
- [23] K. Zhang, T. Mukhriza, X. Liu, P.P. Greco, E. Chiremba, A study on CO2 and CH4 conversion to synthesis gas and higher hydrocarbons by the combination of catalysts and dielectric-barrier discharges, Appl. Catal. A 502 (2015) 138–149.
- [24] X.G. Zheng, S.Y. Tan, L.C. Dong, S.B. Li, H.M. Chen, S.A. Wei, Experimental and kinetic investigation of the plasma catalytic dry reforming of methane over perovskite LaNiO3 nanoparticles, Fuel Process. Technol. 137 (2015) 250–258.
- [25] Y.X. Zeng, L. Wang, C.F. Wu, J.Q. Wang, B.X. Shen, X. Tu, Low temperature reforming of biogas over K-, Mg- and Ce-promoted Ni/Al2O3 catalysts for the production of hydrogen rich syngas: Understanding the plasma-catalytic synergy, Appl Catal B 224 (2018) 469–478.
- [26] W.-J. Jang, H.-M. Kim, J.-O. Shim, S.-Y. Yoo, K.-W. Jeon, H.-S. Na, Y.-L. Lee, D.-W. Jeong, J. Wook Bae, I. Wook Nah, H.-S. Roh, Key properties of Ni–MgO–CeO2, Ni–MgO–ZrO2, and Ni–MgO–Ce(1–x)Zr(x)O2 catalysts for the reforming of methane with carbon dioxide, Green Chemistry. 20 (2018) 1621.
- [27] N. Laosiripojana, W. Sutthisripok, S. Assabumrungrat, Synthesis gas production from dry reforming of methane over CeO2 doped Ni/Al2O3: Influence of the doping ceria on the resistance toward carbon formation, Chem. Eng. J. 112 (2005) 13–22.
- [28] A. Cárdenas-Arenas, E. Bailón-García, D. Lozano-Castelló, P. da Costa, A. Bueno-López, Stable NiO-CeO2 nanoparticles with improved carbon resistance for methane dry reforming, J. Rare Earths 40 (2022) 57–62.
- [29] J. Li, Z. Liu, D.A. Cullen, W. Hu, J. Huang, L. Yao, Z. Peng, P. Liao, R. Wang, Distribution and valence state of Ru species on CeO2 supports: support shape effect and its influence on CO oxidation, ACS Catal. 9 (2019) 11088–11103.
- [30] I.V. Yentekakis, G. Goula, M. Hatzisymeon, I. Betsi-Argyropoulou, G. Botzolaki, K. Kousi, D.I. Kondarides, M.J. Taylor, C.M.A. Parlett, A. Osatiashtiani, G. Kyriakou, J.P. Holgado, R.M. Lambert, Effect of support oxygen storage capacity on the catalytic performance of Rh nanoparticles for CO2 reforming of methane, Appl. Catal. B 243 (2019) 490–501.
- [31] M.R. Ahasan, M.M. Hossain, X. Ding, R. Wang, Non-equilibrium plasma-assisted dry reforming of methane over shape-controlled CeO2 supported ruthenium catalysts, J. Mater. Chem. A Mater. 11 (2023) 10993–11009.
- [32] S. Azam, Z. Wei, R. Wang, Adsorption-catalysis design with cerium oxide nanorods supported nickel-cobalt-oxide with multifunctional reaction interfaces for anchoring polysulfides and accelerating redox reactions in lithium sulfur battery, J. Colloid Interface Sci. 635 (2023) 466–480.
- [33] S. Azam, Z. Wei, R. Wang, Cerium oxide nanorods anchored on carbon nanofibers derived from cellulose paper as effective interlayer for lithium sulfur battery, J. Colloid Interface Sci. 615 (2022) 417–431.
- [34] Y. Wang, R. Wang, Effects of chemical etching and reduction activation of CeO2 nanorods supported ruthenium catalysts on CO oxidation, J. Colloid Interface Sci. 613 (2022) 836–846.
- [35] Y. Wang, Z. Liu, R. Wang, NaBH4 surface modification on CeO2 nanorods supported transition-metal catalysts for low temperature CO oxidation, ChemCatChem 12 (2020) 4304–4316.
- [36] R. Wang, R. Dangerfield, Seed-mediated synthesis of shape-controlled CeO2 nanocrystals, RSC Adv. 4 (2013) 3615–3620.
- [37] Z. Liu, R. Wang, Investigation and Rational design of the catalyst-support interface in, Redox Catalysis by Ceria (2020). https://www.proquest.com/dissertations-the ses/investigation-rational-design-catalyst-support/docview/2426532667/se-2? accountid=14472.
- [38] R.V. Ranganathan, M.M. Hossain, S. Talukdar, R. Ahasan, R. Wang, M. Uddi, Tunable quantum cascade laser absorption spectroscopy for plasma assisted oxidative coupling of methane to C 2 based products, in: In: 2021 IEEE International Conference on Plasma Science (ICOPS), 2021, p. 1.

- [39] A. Löfberg, J. Guerrero-Caballero, T. Kane, A. Rubbens, L. Jalowiecki-Duhamel, Ni/CeO2 based catalysts as oxygen vectors for the chemical looping dry reforming of methane for syngas production, Appl Catal B 212 (2017) 159–174.
- [40] Y. Xie, J. Chen, X. Wu, J. Wen, R. Zhao, Z. Li, G. Tian, Q. Zhang, P. Ning, J. Hao, Frustrated lewis pairs boosting low-temperature CO 2 methanation performance over Ni/CeO 2 nanocatalysts, ACS Catal. 12 (2022) 10587–10602.
- [41] Z. Wei, R. Wang, Chemically etched CeO2-x nanorods with abundant surface defects as effective cathode additive for trapping lithium polysulfides in Li-S batteries, J. Colloid Interface Sci. 615 (2022) 527–542.
- [42] Z. Liu, Y. Lu, M.P. Confer, H. Cui, J. Li, Y. Li, Y. Wang, S.C. Street, E.K. Wujcik, R. Wang, Thermally Stable RuO x-CeO2 nanofiber catalysts for low-temperature CO oxidation, ACS Appl Nano Mater. 3 (2020) 8403–8413.
- [43] L. Liu, Z. Yao, Y. Deng, F. Gao, B. Liu, L. Dong, Morphology and crystal-plane effects of nanoscale ceria on the activity of CuO/CeO2 for NO reduction by CO, ChemCatChem 3 (2011) 978–989.
- [44] M.R. Ahasan, Y. Wang, R. Wang, In situ DRIFTS and CO-TPD studies of CeO2 and SiO2 supported CuOx catalysts for CO oxidation, Mol. Catal. 518 (2022), 112085.
- [45] Y. Wang, Z. Liu, M.P. Confer, J. Li, R. Wang, In-situ DRIFTS study of chemically etched CeO2 nanorods supported transition metal oxide catalysts, Mol. Catal. 509 (2021), 111629.
- [46] A.L.A. Marinho, F.S. Toniolo, F.B. Noronha, F. Epron, D. Duprez, N. Bion, Highly active and stable Ni dispersed on mesoporous CeO2-Al2O3 catalysts for production of syngas by dry reforming of methane, Appl Catal B 281 (2021), 119459.
- [47] N. Yisup, Y. Cao, W.L. Feng, W.L. Dai, K.N. Fan, Catalytic oxidation of methane over novel Ce-Ni-O mixed oxide catalysts prepared by oxalate gel-coprecipitation, Catal Letters. 99 (2005) 207–213.
- [48] G.I. Siakavelas, N.D. Charisiou, S. AlKhoori, A.A. AlKhoori, V. Sebastian, S. J. Hinder, M.A. Baker, I.V. Yentekakis, K. Polychronopoulou, M.A. Goula, Highly selective and stable nickel catalysts supported on ceria promoted with Sm2O3, Pr2O3 and MgO for the CO2 methanation reaction, Appl. Catal. B 282 (2021), 119562.
- [49] A. Cárdenas-Arenas, A. Quindimil, A. Davó-Quiñonero, E. Bailón-García, D. Lozano-Castelló, U. De-La-Torre, B. Pereda-Ayo, J.A. González-Marcos, J. R. González-Velasco, A. Bueno-López, Isotopic and in situ DRIFTS study of the CO2 methanation mechanism using Ni/CeO2 and Ni/Al2O3 catalysts, Appl Catal B 265 (2020), 118538.
- [50] A. Cárdenas-Arenas, A. Quindimil, A. Davó-Quiñonero, E. Bailón-García, D. Lozano-Castelló, U. De-La-Torre, B. Pereda-Ayo, J.A. González-Marcos, J. R. González-Velasco, A. Bueno-López, Design of active sites in Ni/CeO2 catalysts for the methanation of CO2: tailoring the Ni-CeO2 contact, Appl. Mater. Today 19 (2020), 100591.
- [51] M. Hołub, On the measurement of plasma power in atmospheric pressure DBD plasma reactors, Int. J. Appl. Electromagn. Mech. 39 (2012) 81–87.
- [52] Y.R. Luo, Comprehensive handbook of chemical bond energies, Comprehensive Handbook Chem. Bond Energies. (2007) 1–1656.
- [53] A.I. Tsiotsias, N.D. Charisiou, V. Sebastian, S. Gaber, S.J. Hinder, M.A. Baker, K. Polychronopoulou, M.A. Goula, A comparative study of Ni catalysts supported on Al2O3, MgO–CaO–Al2O3 and La2O3–Al2O3 for the dry reforming of ethane, Int. J. Hydrogen Energy 47 (2022) 5337–5353.
- [54] O. Demoulin, B. Le Clef, M. Navez, P. Ruiz, Combustion of methane, ethane and propane and of mixtures of methane with ethane or propane on Pd/γ-Al2O3 catalysts, Appl. Catal. A 344 (2008) 1–9.
- [55] J. Niu, C. Zhang, H. Liu, Y. Jin, R. Zhang, Enhanced performance of oxygen vacancies on CO2 adsorption and activation over different phases of ZrO2, Frontiers in Energy 2023 (2023) 1–10.
- [56] S.N.A. Rosli, S.Z. Abidin, O.U. Osazuwa, X. Fan, Y. Jiao, The effect of oxygen mobility/vacancy on carbon gasification in nano catalytic dry reforming of methane; a review, J. CO2 Util. 63 (2022), 102109.
- [57] Water-gas shift reaction Wikipedia, (n.d.). https://en.wikipedia.org/wiki/Water %E2%80%93gas\_shift\_reaction (accessed December 22, 2022).
- [58] R.V. Ranganathan, Z. Liu, H. Menon, S. Talukdar, R. Wang, M. Uddi, Nanoshaped CeO 2 and SiO 2 supported Ru catalyst for plasma catalysis chemical looping reactions, Int. J. Energy Eng. 2020 (2020) 67–79.
- [59] V.M. Gonzalez-Delacruz, F. Ternero, R. Pereñíguez, A. Caballero, J.P. Holgado, Study of nanostructured Ni/CeO2 catalysts prepared by combustion synthesis in dry reforming of methane, Appl. Catal. A 384 (2010) 1–9.